(12)

SGI-R-83-083

THREE-DIMENSIONAL WAVE PROPAGATION USING BOUNDARY INTEGRAL EQUATION TECHNIQUES

Randy J. Apsel
R. Kipper Wyss
George R. Mellman
Robert S. Hart

AD A124956

"Original contains color plates: All DTIC reproductions will be in black and white"

Final Technical Report.
Sponsored By:
Defense Advanced Research Projects Agency (DoD)
ARPA Order No. 4042

DTIC FILE COPY

Monitored by Naval Ocean Research and Development Activity Under Contract N00014-81-C-0148.

The views and conclusions contained in this document are those of the authors and should not be interpreted as representing the Advanced Research Projects Agency, the Naval Ocean Research and Development activity, or the U.S. Government.

DISTRIBUTION STATEMENT A
Approved for public release;
Distribution Unlimited

January 1983

DTIC
SELECTE
FEB 28 1983
D
B

SIERRA GEOPHYSICS
15446 BELL-RED ROAD, SUITE 400 • REDMOND, WASHINGTON 98052 • (206) 881-8833

83 02 022 044

UNCLASSIFIED

SECURITY CLASSIFICATION OF THIS PAGE (*When Data Entered*)

REPORT DOCUMENTATION PAGE	READ INSTRUCTIONS BEFORE COMPLETING FORM
1. REPORT NUMBER 2. GOVT ACCESSION NO. A124956	3. RECIPIENT'S CATALOG NUMBER
4. TITLE (*and Subtitle*) Three-Dimensional Wave Propagation Using Boundary Integral Equation Techniques	5. TYPE OF REPORT & PERIOD COVERED Final Technical Report October 1980 - Sept. 1982 6. PERFORMING ORG. REPORT NUMBER SGI-R-83-083
7. AUTHOR(s) Randy J. Apsel R. Kipper Wyss George R. Mellman Robert S. Hart	8. CONTRACT ~~OR GRANT~~ NUMBER(s) N00014-81-C-0148
9. PERFORMING ORGANIZATION NAME AND ADDRESS Sierra Geophysics, Inc. 15446 Bell-Red Rd., #400 Redmond, WA 98052	10. PROGRAM ELEMENT, PROJECT, TASK AREA & WORK UNIT NUMBERS ARPA Order No. 4042
11. CONTROLLING OFFICE NAME AND ADDRESS DARPA 1400 Wilson Blvd. Arlington, VA 22209	12. REPORT DATE January 1983 13. NUMBER OF PAGES 72
14. MONITORING AGENCY NAME & ADDRESS(*if different from Controlling Office*) Office of Naval Research Dept. of the Navy 800 N. Quincy St., Arlington, VA 22217	15. SECURITY CLASS. (*of this report*) Unclassified 15a. DECLASSIFICATION/DOWNGRADING SCHEDULE

16. DISTRIBUTION STATEMENT (*of this Report*)

Unlimited

DISTRIBUTION STATEMENT A
Approved for public release;
Distribution Unlimited

17. DISTRIBUTION STATEMENT (*of the abstract entered in Block 20, if different from Report*)

18. SUPPLEMENTARY NOTES

19. KEY WORDS (*Continue on reverse side if necessary and identify by block number*)

wave propagation	irregular interfaces
boundary integral equations	viscoelastic
three-dimensional	near-source structural effects
multilayered	

20. ABSTRACT (*Continue on reverse side if necessary and identify by block number*)

The Boundary Integral Equation (BIE) approach for simulating wave propagation in three-dimensional, irregular multilayered, viscoelastic media is formulated. ~~in this final technical report~~ The BIE formulation takes advantage of known wave propagation properties within an individual layer, leaving only the interactions at the layer boundaries to be treated numerically. This essentially reduces the problem by one spatial dimension and represents a concise treatment of the pertinent physics involved. The resulting system of singular boundary integral equations is much smaller and

DD FORM 1 JAN 73 1473 EDITION OF 1 NOV 65 IS OBSOLETE

UNCLASSIFIED

SECURITY CLASSIFICATION OF THIS PAGE (*When Data Entered*) cont.

than the corresponding system of equations using the Finite Difference or Finite Element approach, but the block diagonal matrices are much more dense.

Two methods are presented for dealing with these dense matrix equations. First an approximate Kirchhoff technique is derived in which only local values of the wave field are allowed to interact with the layer boundaries and the propagation through multilayered structures is accomplished by cascading up and down through the stack to get higher order reflections. Since the Kirchhoff approximation is not valid for critical reflections and some diffraction effects, a second and more complete BIE solution technique was ~~has been~~ developed which iteratively deals with the singular matrix equation from a perturbation point of view with respect to known flat layer solutions.

Sample applications of the Kirchhoff solution technique include a study in which the observed variations in amplitude and waveform of signals recorded across the Northern portion of Yucca Flats at NTS are explained in terms of the near-source structural effects. In the southern portion of the basin, the steeply dipping sidewalls cause the Kirchhoff approximation to be inadequate in explaining the observed motions.

Comparisons are presented between the Kirchhoff solution and the iterative BIE solution showing the inadequacies of the Kirchhoff approximation and the convergence aspects of iterative BIE approach. Sample applications of the iterative BIE solution technique include sensitivity studies in the time and frequency domains on various model parameters such as severity of the surface irregularities, angle of incident energy, impedance contrast across interface and layer thickness.

While the Kirchhoff algorithm is a fully three dimensional code for any number of layers, the current iterative BIE algorithm solves a more specialized class of problems and planned extensions to the general case are outlined in the report.

RE: Classified Reference, Distribution Unlimited
No change per Mr. J.A. Ballard,
NORDA/Code 543

DTIC COPY INSPECTED

Accession For
NTIS GRA&I ☑
DTIC TAB ☐
Unannounced ☐
Justification
By
Distribution/
Availability Codes

Dist	Avail and/or Special
A	

THREE-DIMENSIONAL WAVE PROPAGATION USING
BOUNDARY INTEGRAL EQUATION TECHNIQUES

Randy J. Apsel
R. Kipper Wyss
George R. Mellman
Robert S. Hart

Final Technical Report.
Sponsored By:
Defense Advanced Research Projects Agency (DoD)
ARPA Order No. 4042

Monitored by Naval Ocean Research and Development Activity Under Contract N00014-81-C-0148.

The views and conclusions contained in this document are those of the authors and should not be interpreted as representing the Advanced Research Projects Agency, the Naval Ocean Research and Development activity, or the U.S. Government.

January 1983

SGI-R-83-083

TABLE OF CONTENTS

Page

1.0 INTRODUCTION. 3

2.0 GENERAL FORMULATION OF BIE METHODOLOGY. 7

3.0 SOLUTION USING MODIFIED KIRCHHOFF APPROXIMATION . 19

3.1 Methodology. 19
3.2 Results. 28

4.0 SOLUTION USING RIGOROUS ITERATIVE BIE APPROACH . 38

4.1 Methodology. 38
4.2 Results. 45

5.0 RECOMMENDED EXTENSIONS OF ITERATIVE BIE ALGORITHM 65

6.0 REFERENCES. 67

APPENDIX A. Infinite-space Green's Functions. 69

1.0 INTRODUCTION

Motivated by the increasing demands on theoretical seismology to understand and explain the propagation of waves in complex environments, much research has been devoted over the last few years to developing computationally efficient techniques with as much generality as possible. Although the differential equations of motion are linear in the field quantities of interest, they are non-linear in terms of the boundary conditions for most realistic structures. This fundamental nonlinearity precludes construction of the solution for complex structures by superpositon of the solutions for simple structures, and forces one into computationally costly schemes.

Techniques for dealing with this fundamental nonlinearity have spanned the range from the crudest classical ray tracing approach to the computational-bound finite difference type methods. However, no single technique has ever proven entirely satisfactory for reasons of accuracy, completeness of solution, generality of application, cost or combinations thereof. For example, in cases where significant diffraction and interference effects require "exact" solutions, finite difference techniques have received widespread use. Yet, the finite difference approach is well known for its cumbersome computational demands in two dimensions and almost insurmountable computational demands in three dimensions even on the fastest computers available today.

The heavy computation requirements of the finite difference type methods are created by the necessity of refining the numerical grid proportionately to the wavelengths of interest in all spatial directions, including regions of constant material properties. For problems involving wave propagation in irregular layers of constant material properties within each layer, however, the Boundary Integral Equation (BIE) approach provides a more concise and efficient formulation. Basically, the BIE formulation takes advantage of the fact that the propagation of waves through a region of constant material properties can be treated analytically, leaving only the interactions at the bounding surfaces to be treated numerically. Rather than imposing a grid over the entire volume, the BIE method only requires gridding of the interfaces between regions of constant material properties. Not only are there potential savings in computational effort to solve a smaller systems of equations, but the formulation represents a concise treatment of the pertinent physics involved. By virtue of this contraction of information, the smaller matrices in the BIE formulations are much denser than the corresponding matrices in the finite difference approach. These dense matrices are typically poorly conditioned and must be given careful consideration during implementation of matrix solution techniques to avoid numerical instabilities.

Various techniques have appeared in the literature for dealing with the dense matrices in the BIE approach. One technique involves introduction of a Kirchhoff approximation into the BIE formalism (eg., Berryhill, 1979; Scott and Helmberger, 1982). In the Kirchhoff approximation the interaction between neighboring points on a boundary is ignored by locally approximating the boundary at each sample point by the tangent plane at that point and then using plane wave reflection and transmission coefficients to compute the unknown boundary values. Sierra Geophysics has added two important modifications to this classical Kirchhoff approximation: (1) definition of a locally equivalent incident pulse from the neighboring boundary allowing for some diffraction effects which would otherwise be neglected; (2) formulation in terms of a series of two-layer problems allowing higher order multiples to be computed by recursively propagating the boundary values up and down the stack of layers so that the computational cost increases proportionately to the number of layers rather than the square of the number of layers.

Even with the improved Kirchhoff approximation, one is still confronted with the poor conditioning and denseness of the matrices used to propagate the boundary values forward to the desired positions. Also, waves involving multiple interactions with a single boundary are neglected except for the pseudo-diffraction effects which are not exact. Therefore more rigorous techniques are required to deal with the full system of boundary integral equations. A time domain treatment of the full system of equations has been successfully addressed by Cole (1980) for two-dimensional acoustical problems in geophysics. Cole's approach becomes expensive at high frequencies or for late arriving signals as the product of the frequency step times the time step must be less than about 10 to maintain stability. More importantly, the formulation does not handle the dense matrices efficiently, precluding generalization to three-dimensional elastic multilayered problems. Also, it is difficult to include realistic material attenuation and to suppress late arriving spurious reflections off the artificial extremities of the grid using a time domain formulation. Significant breakthroughs have been made at Sierra Geophysics in deriving an iterative frequency domain treatment of the full system of equations that overcomes these shortcomings.

The iterative BIE treatment deals with the dense singular matrix equations from a perturbation point of view with respect to the flat layer solution. Using the perturbation approach, all inverse matrix operations are reduced to simpler deconvolution operations, which are optimally handled using Fourier transform algorithms. Also, spurious edge effects are either removed completely or to first order (in which case Fourier tapering is used to remove higher order effects) depending on the slope of the extremities of the boundaries. Another feature that makes three-dimensional problems feasible with the frequency domain approach is the computational savings experienced in varying the numerical grid spacing as a function of frequency reducing the size of the matrix equations at low frequency relative to high frequency. Furthermore, geometrical spreading and material attenuation behavior can be invoked at high frequency where appropriate to reduce the size of the matrix equations by eliminating the noncontributing interaction terms. This has the desirable feature of allowing the iterative BIE solution to execute as efficiently as the approximate Kirchhoff or geometrical ray solutions in the high frequency limit.

The basic methodology common to all the BIE techniques is presented in Chapter 2. The formulation is completely general for three-dimensional elastic media containing any number of irregularly shaped layers including the limit of zero thickness pinchouts. A discrete grid is imposed and the resulting BIE matrix equations are discussed in terms of denseness and singularity considerations. The Kirchhoff BIE solution technique developed at Sierra Geophysics as discussed above is presented in Section 3.1 including the enhancements to include pseudo-diffraction effects and permit linear cost dependence on the number of layers. Sample problems solved with this Kirchhoff technique are presented in Section 3.2. The more exact iterative BIE solution technique developed at Sierra Geophysics as discussed above is presented in Section 4.1. Sample problems solved with the iterative BIE technique are presented in Figure 4.2 including comparisons showing the deficiencies of the Kirchoff technique as well as the convergence behavior of the iterative approach. A brief discussion of the current status and future extensions of the iterative BIE technique is discussed in Chapter 5 with a reference list following in Chapter 6.

2.0 GENERAL FORMULATION OF BIE METHODOLOGY

The boundary integral equations describing wave propagation through arbitrary three-dimensional elastic multilayered media are derived in two steps. First, the known characterization of wave propagation within a single irregular layer is written in terms of integral representations involving the full space Green's functions with properties of that layer. Second, the interaction of the wavefield is simultaneously imposed at all boundaries to satisfy all boundary and continuity conditions leading to a system of Fredholm integral equations of the second kind for the unknown boundary values. Once this system of equations is solved for the boundary values, the wavefield may be propagated from the boundaries to all receiver positions of interest within a given layer using the integral representations of the first step.

The model geometry for the wave propagation problem solved in the BIE formulation is depicted in Figure 1 by N irregular layers overlying a semi-infinite half-space. The layers are allowed to pinchout but not to cross in this formulation. Each layer is characterized by constant shear and compressional wave velocities and constant densities. Material attenuation may be introduced by allowing the velocities to be complex. Wave propagation within a given layer is expressed in terms of the Green's functions for a full-space with the properties of that layer. The formulation is not restricted to constant material properties within a given layer, although the Green's functions for that case are quite simple. The formulation is carried out for the full elastic case and the corresponding acoustic formulation is obtainable from the derived equations by replacing the vector equations with scalar equations.

The first step in the formulation is to write expressions for the displacement field within a single layer without consideration of the boundary interaction. In layer ℓ (ℓ=1,2,...,N+1), the displacement vector must satisfy the homogeneous ($\ell \neq s$) or inhomogeneous ($\ell = s$) equations of motion (depending on whether or not the source is located in layer ℓ) for a full space with properties of layer ℓ. The Representation Theorem of Elastodynamics (see, for example, deHoop,

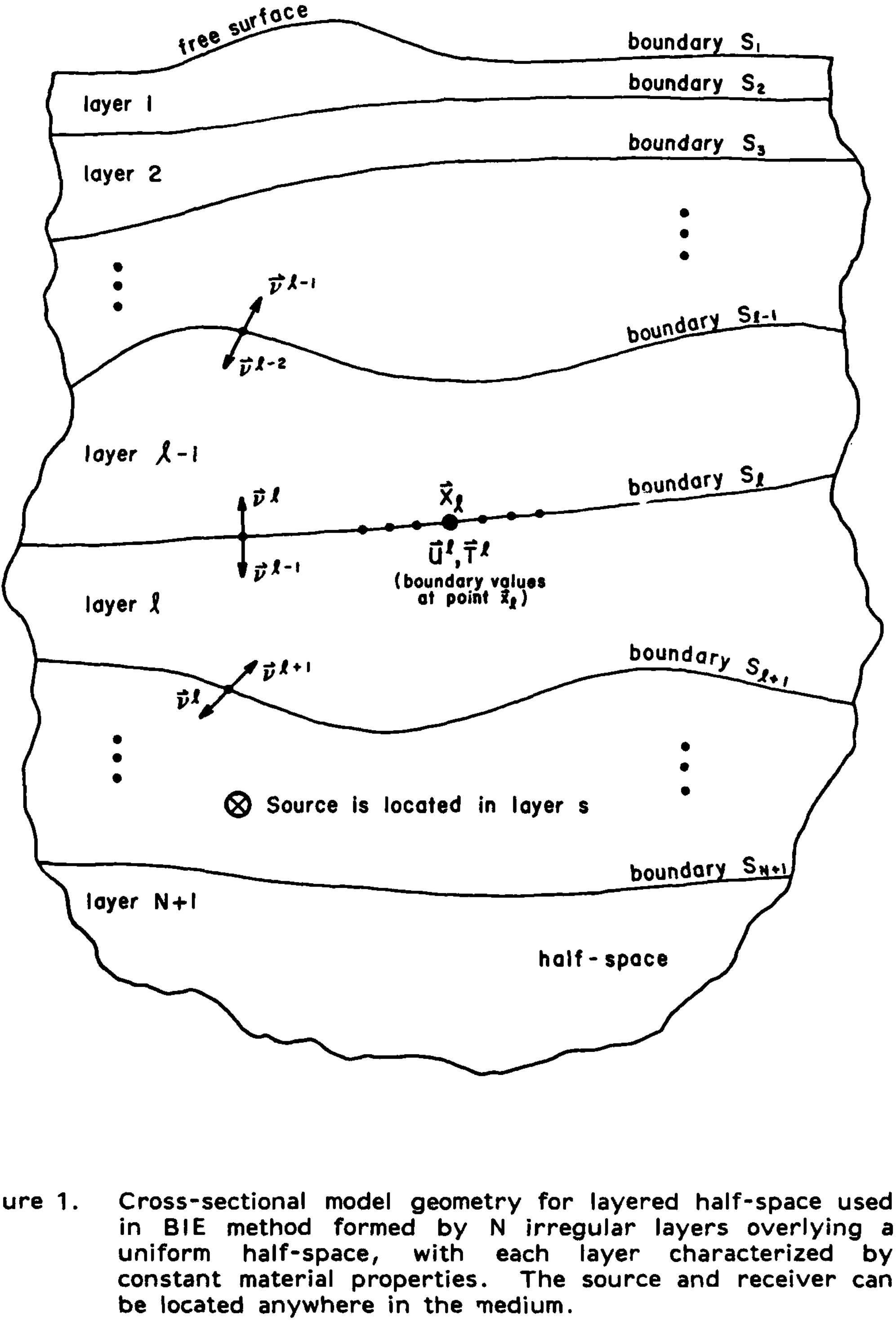
free surface
boundary S_1
boundary S_2
layer 1
boundary S_3
layer 2
$\vec{\nu}^{\ell-1}$
$\vec{\nu}^{\ell-2}$
boundary $S_{\ell-1}$
layer $\ell-1$
$\vec{\nu}^{\ell}$
$\vec{x}_\ell$
boundary S_ℓ
$\vec{\nu}^{\ell-1}$
$\vec{U}^\ell, \vec{T}^\ell$
(boundary values at point $\vec{x}_\ell$)
layer ℓ
$\vec{\nu}^{\ell+1}$
$\vec{\nu}^{\ell}$
boundary $S_{\ell+1}$
Source is located in layer s
boundary S_{N+1}
layer N+1
half-space

Figure 1. Cross-sectional model geometry for layered half-space used in BIE method formed by N irregular layers overlying a uniform half-space, with each layer characterized by constant material properties. The source and receiver can be located anywhere in the medium.

1958) provides an expression for the displacement vector located anywhere within volume V_ℓ containing layer ℓ in terms of integrals of the displacement and traction field over the bounding surface of volume V_ℓ times the corresponding Green's functions for a full-space with properties of that layer. The i-component of displacement at location $\vec{x}_\ell$ can then be written in the frequency domain using the Representation Theorem for a volume V_ℓ bounded by layer interfaces S_ℓ and $S_{\ell+1}$.

$$\begin{aligned}\varepsilon^{\ell}(\vec{x}_\ell)\, U_i^{\ell}(\vec{x}_\ell) = &\int_{S_\ell} \left[G^{\ell}_{ji}(\vec{x}_\ell,\vec{y}_\ell) T^{\ell}_j(\vec{y}_\ell) - H^{\ell}_{ji}(\vec{x}_\ell,\vec{y}_\ell) U^{\ell}_j(\vec{y}_\ell) \right] dS(\vec{y}_\ell) \\ &- \int_{S_{\ell+1}} \left[G^{\ell}_{ji}(\vec{x}_\ell,\vec{y}_{\ell+1}) T^{\ell+1}_j(\vec{y}_{\ell+1}) - H^{\ell}_{ji}(\vec{x}_\ell,\vec{y}_{\ell+1}) U^{\ell+1}_j(\vec{y}_{\ell+1}) \right] dS(\vec{y}_{\ell+1}) \\ &+ \delta_{\ell s} \int_{V_\ell} \left[G^{\ell}_{ji}(\vec{x}_\ell,\vec{z}_\ell) f_j(\vec{z}_\ell) \right] dV(\vec{z}_\ell) \qquad (1) \\ & \qquad\qquad\qquad\qquad (i,j=1,2,3)\end{aligned}$$

in which the summation over repeated indices is understood, the frequency arguments have been omitted for brevity and

$\vec{y}_m$ = an integration point on bounding surface S_m;

$G^{\ell}_{ji}(\vec{x}_\ell,\vec{y}_m)$ = the j-component of the full-space Green's function displacement vector at location $\vec{y}_m$ on surface S_m due to point force in the i-direction at location $\vec{x}_\ell$ with properties of layer ℓ;

$H^{\ell}_{ji}(\vec{x}_\ell,\vec{y}_m)$ = the j-component of the corresponding Green's function traction vector formed from the inner-product of the kj-component of the Green's function stress tensor G^{ℓ}_{kji} at location $\vec{y}_m$ on surface S_m with the k-component of the unit upward normal ν^m_k at point $\vec{y}_m$ (summing over k=1,2,3);

$U_j^m(\vec{y}_m)$ = the j-component of displacement at location y_m on surface S_m;

$T_j^m(\vec{y}_m)$ = the j-component of the corresponding traction at location $\vec{y}_m$ on surface S_m formed from the inner-product of the kj-component of the stress tensor with the k-component of the unit upward normal $\vec{v}_k^m$ at point $\vec{y}_m$ (summing over k=1,2,3);

$f_j(\vec{z}_\ell)$ = the j-component of the source function at location $\vec{z}_\ell$ anywhere in layer ℓ (assuming the source is a Delta-function in space, then the volume integral reduces to the evaluation of the integrand at point $\vec{z}_\ell$);

$$\delta_{\ell s} = \begin{cases} 0, & \text{if } l \neq s \\ 1, & \text{if } l = s \end{cases} \quad , s = \text{source layer number;}$$

$$\varepsilon^{\ell}(\vec{x}_\ell) = \begin{cases} 1, & \text{if } \vec{x}_\ell \text{ inside layer } \ell \\ \tfrac{1}{2}, & \text{if } \vec{x}_\ell \text{ on surface bounding layer } \ell \\ 0, & \text{if } \vec{x}_\ell \text{ outside layer } \ell. \end{cases}$$

In Eq. (1), the layer comprising volume V_ℓ is assumed to extend to infinity at the horizontal extremes to eliminate the surface integrals along those portions of the surface bounding volume V_ℓ and the negative sign for the integral over surface $S_{\ell+1}$ is associated with using the upward normal $\vec{v}^{\ell+1} = -\vec{v}^{\ell}$ in the definition of the traction components. Once the boundary values for $U_j^m(\vec{y}_m)$ and $T_j^m(\vec{y}_m)$ are determined for bounding interfaces S_ℓ and $S_{\ell+1}$, Eq. (1) can then be used to obtain the displacement field at any point $\vec{x}_\ell$ within layer ℓ. Expressions for the full-space Green's functions with constant material properties are given in Appendix A for two and three dimensional wave propagation in elastic as well as acoustic media. This completes the propagation step of the BIE formulation and what remains is to impose the boundary interaction coupling.

The boundary interaction coupling requires simultaneous satisfaction of a tractionless free surface (interface 1) and continuous displacements and tractions across each layer interface (2,3,...,N+1). The coupled boundary integral equations arising from the zero tractions conditions along the free surface are obtained by evaluating Eq. (1) in volume V_1 (layer 1) at a discrete number (q_1) of observation points $\vec{x}_1$ along surface S_1 and imposing the zero traction condition $T_j^1(\vec{y}_1) = 0$ (j=1,2,3) for all quadrature points $\vec{y}_1$ on surface S_1 to yield:

$$
\begin{aligned}
\frac{1}{2}\, U_i^1(\vec{x}_1) = & - \int_{S_1} \left[H_{ji}^1(\vec{x}_1,\vec{y}_1) U_j^1(\vec{y}_1) \right] dS(\vec{y}_1) \\
& - \int_{S_2} \left[G_{ji}^1(\vec{x}_1,\vec{y}_2) T_j^2(\vec{y}_2) - H_{ji}^1(\vec{x}_1,\vec{y}_2) U_j^2(\vec{y}_2) \right] dS(\vec{y}_2) \\
& + \delta_{1,s} F_i(\vec{x}) \quad , \qquad (i,j=1,2,3), \qquad (2)
\end{aligned}
$$

in which the direct source contribution (if s=1) is

$$
F_i(\vec{x}_1) = \int_{V_1} \left[G_{ji}^1(\vec{x}_1,\vec{z}_1) f_j(\vec{z}_1) \right] dV(\vec{z}_1). \qquad (3)
$$

Equations (2) represent a simultaneous set of $3q_1$ Fredholm integral equations of the second kind for the same number of unknown displacement boundary values U_j^1, j=1,2,3, on surface S_1, which are coupled to the unknown boundary values on surface S_2 through the integral over surface S_2. Note that if half-space Green's functions were used in layer 1 instead of the full-space Green's functions, then the terms involving the traction Green's function, H_{ji}^1, would not be present leading to a simpler form of the free surface boundary integral equations. However, analytic expressions for the half-space Green's functions are only available for a special class of two-dimensional problems and hence will not be introduced for layer 1 to maintain generality and consistency in the formulation.

The coupled boundary integral equations arising from the continuity conditions across each layer interface, S_ℓ (ℓ=2,3,...,N+1), are obtained by evaluating Eq. (1) in volumes $V_{\ell-1}$ and V_ℓ (layers ℓ-1 and ℓ) at a discrete number (q_ℓ) of observations $\vec{x}_\ell$ along common surface S_ℓ and imposing the natural boundary conditions of continuous displacements and tractions:

$$U_j^{\ell-1}(\vec{x}_\ell) = U_j^\ell(\vec{x}_\ell) \quad \text{and} \quad T_j^{\ell-1}(\vec{x}_\ell) = T_j^\ell(\vec{x}_\ell)$$

for j=1,2,3 and for all quadrature points $\vec{y}_\ell$ on surface S_ℓ to yield:

$$\frac{1}{2}U_i^\ell(\vec{x}_\ell) = \int_{S_{\ell-1}} \left[G_{ji}^{\ell-1}(\vec{x}_\ell,\vec{y}_{\ell-1})T_j^{\ell-1}(\vec{y}_{\ell-1}) - H_{ji}^{\ell-1}(\vec{x}_\ell,\vec{y}_{\ell-1})U_j^{\ell-1}(\vec{y}_\ell)\right] dS(\vec{y}_{\ell-1})$$

$$- \int_{S_\ell} \left[G_{ji}^{\ell-1}(\vec{x}_\ell,\vec{y}_\ell)T_j^{\ell-1}(\vec{y}_\ell) - H_{ji}^{\ell-1}(\vec{x}_\ell,\vec{y}_\ell)U_j^{\ell-1}(\vec{y}_\ell)\right] dS(\vec{y}_\ell)$$

$$+ \delta_{\ell-1,s}F_i(\vec{x}_\ell) \qquad (4a)$$

and

$$\frac{1}{2}U_i^\ell(\vec{x}_\ell) = \int_{S_\ell} \left[G_{ji}^\ell(\vec{x}_\ell,\vec{y}_\ell)T_j^\ell(\vec{y}_\ell) - H_{ji}^\ell(\vec{x}_\ell,\vec{y}_\ell)U_j^\ell(\vec{y}_\ell)\right] dS(\vec{y}_\ell)$$

$$- \int_{S_{\ell-1}} \left[G_{ji}^\ell(\vec{x}_\ell,\vec{y}_{\ell+1})T_j^\ell(\vec{y}_{\ell+1}) - H_{ji}^\ell(\vec{x}_\ell,\vec{y}_{\ell+1})U_j^\ell(\vec{y}_{\ell+1})\right] dS(\vec{y}_{\ell+1})$$

$$+ \delta_{\ell,s}F_i(\vec{x}_\ell) \quad , \quad (i,j=1,2,3),\ (\ell=2,3,\ldots,N+1). \qquad (4b)$$

Equations (4) represent a simultaneous set of $6q_\ell$ Fredholm integral equations of the second kind for the same number of unknown displacement and traction boundary values, U_j^ℓ and T_j^ℓ, j=1,2,3, on surface S_ℓ, which are coupled to the unknown boundary values on surface $S_{\ell-1}$

and $S_{\ell+1}$ through the integrals over surfaces $S_{\ell-1}$ and $S_{\ell+1}$, respectively. Note that when ℓ=2 in Eqs. (4a), then the term involving $T_j^{\ell-1}(\vec{y}_{\ell-1})$ is identically zero because of the tractionless free surface conditions. Also, note that when ℓ=N+1 in Eqs. (4b), then the integral over surface $S_{\ell+1}$ vanishes by virtue of the radiation conditions implicit in the Green's functions for the underlying semi-infinite space. Boundary integral equations (2) and (4) are evaluated at a discrete set of q_ℓ example points $\vec{x}_\ell$ on each boundary S_ℓ with sample points from one boundary becoming Green's function quadrature points for the next boundary. When completely discretized, equations (2) and (4) represent a coupled system of singular Fredholm integral equations of the second kind for the unknown boundary values along all layer boundaries. The singularities occur in the Green's functions when quadrature point $\vec{y}_m$ approaches observation point $\vec{x}_m$ in the second integral in Eqs. (4a) and the first integral in Eqs. (2) and (4b). Singularities can also occur in the Green's functions when two adjacent layer boundaries intersect and would be evidenced in the first integral in Eqs. (4a) or the second integral of Eqs. (2) or (4b), depending on where the intersections occur. An equivalent BIE formulation using integral representations for the traction components as well as the displacement components leads to a system of Fredholm integral equations of the first kind instead of the second kind. At first this appears to be a simpler formulation, but in fact requires more bookkeeping and computational effort in dealing with the higher order singularities arising from the derivations of the stress Green's function components. The singularities are of the lowest order possible using the present BIE formulation in terms of Fredholm integral equations of the second kind and are rigorously handled using the iterative BIE solution technique discussed in Section 4.1.

To complete the general formulation, the discretized boundary integral equations are cast into matrix form:

$$[I]\{U\} = [H]\{U\} - [G]\{T\} + \{F\} \quad . \tag{5}$$

The vectors $\{U\}$ and $\{T\}$ contain all the unknown boundary values along all layer boundaries:

$$\{U\} = \{U_1\},\{U_2\}\ldots,\{U_{N+1}\} \;;\; \{T\} = \{T_2\},\{T_3\}\ldots,\{T_{N+1}\}$$

in which $\{U_\ell\}$ are subvectors containing the $3q_\ell$ unknown displacement boundary values along interface ℓ ($\ell=1,2,\ldots,N+1$) and $\{T_\ell\}$ are subvectors containing the $3q_\ell$ unknown traction boundary values along interface ℓ ($\ell=2,3,\ldots,N+1$). The vector $\{F\}$ contains the direct source contributions along interfaces s and s-1 above and below source layer s:

$$\{F\} = \{0\},\{0\},\ldots,\{F_s\},\{F_{s+1}\},\{0\},\{0\},\ldots$$

in which $\{F_s\}$ is the subvector containing the direct upgoing source field evaluated at $3q_s$ sample points in Eqs. (2) or (4b) depending on whether $s=1$ or $s=2,3,\ldots,N+1$, respectively, and $\{F_{s+1}\}$ is the subvector containing the direct downgoing source field evaluated at $3q_{s+1}$ sample points in Eqs. (4a) if $s=1,2,\ldots,N$.

The matrix $[I]$ contains the factors of (1/2) from the left-hand sides of Eqs. (2) and (4) and is of the following block diagonal form:

$$[I] = \frac{1}{2}\begin{bmatrix}
[I_1] & & & & & \\
& [I_2] & & & \bigcirc & \\
& [I_2] & & & & \\
& & [I_3] & & & \\
& & [I_3] & & & \\
& & & \ddots & & \\
& \bigcirc & & & & \\
& & & & [I_N] & \\
& & & & [I_N] & \\
& & & & & [I_{N+1}] \\
& & & & & [I_{N+1}]
\end{bmatrix}$$

in which $[I_\ell]$ are $3q_\ell \times 3q_\ell$ identity submatrices ($\ell=1,2,\ldots,N+1$); all other submatrices of $[I]$ are zero. The matrix $[H]$ contains the traction

Green's function components times the quadrature coefficients from the discretized integrals in Eqs. (2) and (4) and is of the following block tri-diagonal form:

$$
[H] = \begin{bmatrix}
[-H^{1}_{1,1}] & [H^{1}_{1,2}] & & & & & & & \\
[-H^{1}_{2,1}] & [H^{1}_{2,2}] & & & & & & & \\
 & [-H^{1}_{2,1}] & [H^{1}_{2,2}] & & & & & & \\
 & [-H^{2}_{3,2}] & [H^{2}_{3,3}] & & & & & \Large 0 & \\
 & & [-H^{3}_{3,3}] & [H^{3}_{3,4}] & & & & & \\
 & & & \ddots & & & & & \\
 & & & & [-H^{\ell-1}_{\ell,\ell-1}] & [H^{\ell-1}_{\ell,\ell}] & & & \\
 & & & & & [-H^{\ell}_{\ell,\ell}] & [H^{\ell}_{\ell,\ell+1}] & & \\
 & \Large 0 & & & & & \ddots & & \\
 & & & & & & & [-H^{N}_{N+1,N}] & [H^{N}_{N+1,N+1}] \\
 & & & & & & & & [-H^{N}_{N+1,N+1}]
\end{bmatrix}
$$

in which $[H^{n}_{\ell m}]$ $(m=\ell-1,\ell,\ell+1)$ are $3q_{\ell}\times 3q_{m}$ submatrices involving the traction Green's function components $H^{n}_{ji}(\vec{x}_{\ell},\vec{y}_{m})$ for a full-space with properties of layer n for n=1,2,...,N+1; all other submatrices of [H] are zero.

The matrix [G] contains the displacement Green's functions times the quadrature coefficients from the discretized integrals in Eqs. (2) and (4) and is of the following block tri-diagonal form:

$$[G] = \begin{bmatrix} [\ G^{1}_{1,2}] & & & & & \\ [\ G^{1}_{2,2}] & & & & & \\ [-G^{1}_{2,1}] & [\ G^{1}_{2,2}] & & & & \\ [-G^{2}_{3,2}] & [\ G^{2}_{3,3}] & & & \mathbf{O} & \\ & [-G^{3}_{3,3}] & [\ G^{3}_{3,4}] & & & \\ & & \ddots & & & \\ & & [-G^{\ell-1}_{\ell,\ell-1}] & [\ G^{\ell-1}_{\ell,\ell}] & & \\ & & & [-G^{\ell}_{\ell,\ell}] & [\ G^{\ell}_{\ell,\ell+1}] & \\ & & & & \ddots & \\ \mathbf{O} & & & & [-G^{N}_{N+1,N}] & [\ G^{N}_{N+1,N+1}] \\ & & & & & [-G^{N}_{N+1,N+1}] \end{bmatrix}$$

in which $[G^{n}_{\ell m}]$ ($m=\ell-1,\ell,\ell+1$) are $3q_{\ell}\times 3q_{m}$ submatrices involving the displacement Green's function components $G^{n}_{ji}(\vec{x}_{\ell},\vec{y}_{m})$ for a full-space with properties of layer n for $n=1,2,\ldots,N+1$; all other submatrices of [G] are zero and submatrices $[G^{1}_{\ell 1}]$ ($\ell=1,2$) are not used in the formulation because the known zero tractions along the free surface have been removed from the integral equations.

The matrix equation represented by Eq. (5) must be solved at each frequency value of interest for the unknown displacement and traction boundary values {U} and {T} along all discrete sample points. Once solved, the displacement field is easily obtained at additional sample point (if desired) by evaluation Eq. (1) at locations $\vec{x}_{\ell}$ in layer ℓ in terms of the known displacement and traction boundary values from the surrounding layer interfaces. If desired, time histories are obtained through discrete Fourier synthesis by storing the solved boundary values at the required frequency values.

Equation 5 is the so-called dense matrix equation referred to in Chapter 1 and being of lower dimensionality, but higher density than the corresponding matrix equation obtained from full volume gridding in the finite difference of finite element approaches. For purposes of comparing the respective storage requirements only, assume that the number of sample points q_ℓ along all interfaces S_ℓ ($\ell=1,2,\ldots,N+1$) is a constant equal to q. Then the BIE formulation represents a system of (6N+3)q equations for the (6N+3)q unknown boundary values in contrast to being proportional to q^2 in finite difference methods for 2-D calculations, indicating a potentially large savings in computational effort with all other cost parameters held constant. This potential savings is experienced when the number of layers N is less than the number of vertical wavelengths being resolved in the finite difference approach, which is almost always quite substantial especially at high frequencies and/or for deep layered structures. The actual storage requirements for the two techniques are comparable with the BIE formulation having $(72N-18)q^2+(6N+3)q$ nonzero matrix entries and the finite difference formulation also being proportional to q^2 for 2-D calculations. For 3-D calculations, both methods add another multiplicative factor of q to the number of equations and storage requirements, indicating the same amount of potential savings in 3-D as in 2-D for the BIE method. Therefore all that is entailed to reach the full potential in computational savings is being able to efficiently and stably deal with the smaller, but denser, matrices in the BIE formulation.

As mentioned previously, matrix Eq. (5) has singularities arising from the Green's functions when source and receiver point coincide in this formulation. Therefore careful treatment of this dense matrix equation is required to avoid potential numerical instabilities. A modified Kirchhoff solution technique is derived in Section 3.1 for dealing with this dense singular matrix equations in an appropriate manner. Various local and/or high frequency assumptions are made that decouple adjacent sample points on a given layer boundary resulting in an approximate solution applicable where dynamic effects of interaction of the wavefield with a boundary are not important. A more exact iterative BIE solution technique is derived in Section 4.1 by analytically subtracting off the singularities and solving the system of equations from a perturbation point of view with respect to flat layers. The iterative BIE solution technique not only handles the singularities, but includes all boundary interactions and also effectively deals with the denseness of the matrix equations.

3.0 SOLUTION USING MODIFIED KIRCHHOFF APPROXIMATION

In this chapter, a modified Kirchhoff approximation is used to solve the general BIE problem formulated in Chapter 2. The solution technique is described in Section 3.1. Included is a discussion of two important enhancements that make Sierra Geophysics' technique more general and efficient than the conventional Kirchhoff treatments. Also the major shortcomings are discussed such as exclusion of head waves and diffraction of post-critical waves and limitation on the proximity of two adjacent boundaries. For a more rigorous treatment of the general BIE problem, the reader is referred to Chapter 4.

Sample applications are presented in Section 3.2 showing the versatility and flexibility of the Kirchhoff algorithm. In the first example, the Kirchhoff algorithm is used to demonstrate the near-source structural effects on body waves at the Nevada Test Site. In the second example, the Kirchhoff code is used to demonstrate the effects of basins on earthquake strong ground motions. Comparisons to the more rigorous iterative BIE solution are made in Section 4.2.

3.1 Methodology

In the approximate Kirchhoff treatment of the general BIE problem presented in Chapter 2, the interaction of the propagating wavefield with the boundaries is only considered locally with no interaction between neighboring points on a single boundary. At each boundary point, the interaction of the incident wave with the boundary is calculated as though the local portion of the incident wavefield were part of a plane wave and the local portion of the interacting boundary were a flat plane with unit normals defined by the tangent to the local boundary. Thereby the boundary iteraction reduces to simple convolutional form which can be handled analytically allowing the boundary values at that point to be computed from the local direction and amplitude of the equivalent incident plane wave through simple use of plane wave reflection and transmission coefficients. In general, these coefficients change as a function of frequency and position on the boundary. The definition of a pointwise equivalent incident wave field is unique in Sierra Geophysics' Kirchhoff solution technique and is an important enhancement for including some diffraction effects which would otherwise be neglected. The shortcomings in the conventional Kirchhoff approximation arise from propagating the field from each discrete point on the adjacent surface to the local boundary point, calculating the boundary values at that point using the reflection/transmission coefficients and then summing the individual contributions at that point with a significant number of those contributions originating from post-critical angles.

A second feature unique in Sierra Geophysics' Kirchhoff solution technique is the recursive approach to the propagation of the boundary values through a stack of layers. The first step in the recursive procedure is to propagate the source field once through the stack of layers applying the Kirchhoff approximation point by point and saving all the boundary values. Next, the propagation direction is reversed with the upgoing boundary values along surface 1 propagated back down through the stack of layers and/or the downgoing boundary values along surface N+1 propagated back up through the stack of layers. This provides first order reflections and the process of recursively cascading up and down through the stack of layers is repeated, updating the upgoing and downgoing boundary values at each interface until as many orders of multiple reflections are included as desired. The last step is then to combine the updated upgoing and downgoing boundary values at all boundary points from which the boundary values may be propagated to any position(s) of interest within any layer using the Green's function integral representations discussed in step one of the general BIE formulation in Chapter 2. This second unique feature not only reduces the total storage requirements because only two interfaces need be considered simultaneously, but also allows the computational effort to be linearly proportional to both the desired order number of the multiple reflections and the number of layers in the stack (in contrast to the number of layers squared).

This Kirchhoff solution technique may be viewed as a ray expansion for BIE methods and bears a strong resemblance to geometrical optics (see, for example, Hong and Helmberger, 1978). In fact, geometrical optics can be derived as high frequency approximation to the Kirchhoff formulation, indicating that with proper grid resolution, the Kirchhoff approximation will provide highly accurate results in domains where geometrical optics is valid (eg., at high frequency and angles away from critical where there is little communication between adjacent boundary points). In domains where optics breaks down, the Kirchhoff approximation still provides reasonable results. For example, optics gives abrupt, discontinuous behavior at shadow zone boundaries, whereas the Kirchhoff approximation exhibits continuous, frequency dependent behavior expected from diffraction theory. The Kirchhoff solution is most reliable in situations dominated by kinematic effects, becoming increasingly inaccurate (amplitudes more so than arrival times) where dynamic effects become important. These dynamic effects are related to multiple interactions of the wavefield with a boundary such as head waves and diffraction of post-critical waves). In such cases where dynamic effects are important, the more exact iterative BIE solution technique described in Section 4.1 is recommended.

The approximate Kirchhoff solution technique can be derived at a given frequency from the general BIE formulation in Eq. (5) of Chapter 2, although the more conventional derivation is in terms of the equivalent potential field BIE formulation. The basis of the Kirchhoff approximation is to find a set of assumptions that will decouple the interaction of the wavefield at a point on a boundary from all other points on that boundary and cast the equations into convolutional form. This is accomplished by assuming that the boundary is sufficiently smooth in the vicinity of a sample point to locally allow the boundary geometry to be represented by a flat plane with unit normals defined by the tangent at that sample point. By virtue of the local smoothness assumption, the boundary values and Green's functions will be slowly varying as a function of distance from this sample point. In particular, with tangent plane representations of the local boundary geometry, the traction Green's function terms which involve normal derivatives across the boundary may be discarded at all sample points (i.e., the term involving the matrix [H] in Eq. (5) may be discarded). It is further assumed that the tangent plane lies sufficiently close to the global boundary so that the offsets along the normal direction between the tangent plane and the discrete quadrature points may be disregarded so that the integration over the original boundary can be carried out in the local tangent plane coordinates. This reduces all vector inner products of the submatrices $[G^{\ell-1}_{m,\ell}]$, $m=\ell-1,\ell$ and $[G^{\ell}_{m,\ell}]$, $m=\ell,\ell+1$ with subvectors $\{T_\ell\}$, $\ell=2,3,\ldots,N+1$, to simple convolutional form. Therewith, Eq. (5) can be rewritten as

$$[I]\{U\} + [\hat{G}]\{T\} = \{F\} \quad , \qquad (6)$$

in which each row of matrix $[\hat{G}]$ corresponds to the flat plane Green's function operator at a given sample point obtained by rotating and translating the original Cartesian coordinate system into the local tangent plane coordinates. The solution of this system of equations can therefore be handled quite effectively by analytically applying two-dimensional Fourier transforms in the local tangent plane coordinates, reducing the problem to simple deconvolutional division operations.

As an example, the form of the deconvolutional coefficients will be derived for interaction at a boundary in 3-D structures. The Green's functions in the local coordinates x,y of the tangent plane are obtained from Appendix A by letting $R = |\vec{x}-\vec{y}| = (x^2+y^2)^{\frac{1}{2}}$. Then the two-dimensional Fourier transform of the Green's function G(x,y) takes the form

$$g(k_1,k_2) = \int_{-\infty}^{\infty}\int_{-\infty}^{\infty} (1/R)e^{-ik_\alpha R}\, e^{ik_1 x}\, e^{ik_2 y}\, dx\, dy, \qquad (7a)$$

in which k_α is the wavenumber defined by frequency (ω) divided by acoustic velocity (α) of the layer. Then introducing the Sommerfeld representation

$$\frac{e^{-ik_\alpha R}}{R} = \int_0^\infty \frac{k}{(k^2-k_\alpha^2)^{\frac{1}{2}}} J_0(kR)dK \qquad (7b)$$

into Eq. (7a) and using the identity

$$\int_{-\infty}^{\infty} J_0[k(x^2+y^2)^{\frac{1}{2}}]\, e^{ik_1x}\, dx = \begin{cases} \dfrac{2\cos[y(k^2-k_1^2)^{\frac{1}{2}}]}{(k^2-k_1^2)^{\frac{1}{2}}} & , k>k_1 \\ 0 & , 0\leq k\leq k_1 \end{cases} \qquad (7c)$$

to integrate over x leads to:

$$g(k_1,k_2) = \int_{-\infty}^{\infty}\int_{k_1}^{\infty} \frac{2\cos[k^2-k_1^2)^{\frac{1}{2}}]}{(k^2-k_1^2)^{\frac{1}{2}}} \frac{k}{(k^2-k_\alpha^2)^{\frac{1}{2}}}\, e^{ik_2y}\, dk\, dy. \qquad (7d)$$

Finally, introducing the change of variables $k'=(k^2-k_1^2)^{\frac{1}{2}}$, the integral over y in Eq. (7d) requires that $k'=k_2$ for a nontrivial integral leading to the final form for the deconvolutional coefficients in the transform domain:

$$g(k_1,k_2) = 2\pi[k_1^2+k_2^2-k_\alpha^2]^{-\frac{1}{2}} = -2\pi i/v_\alpha \qquad (7e)$$

in which v_α is the vertical wavenumber for acoustic velocity α (i.e., cosine of the angle of emergence divided by α). If one were dealing with potentials instead of displacements and tractions, this would allow the unknown potentials to be solved in terms of the familiar plane wave reflection and transmission coefficients at the artificial tangent plane boundary. For example, consider the solution of the downgoing potential field ϕ_ℓ and its normal derivative $d\phi_\ell/dn$ in the transform domain (k_1,k_2,ω) at each point along a boundary S_ℓ with a source in layer ℓ-1. The pair of boundary integral equations for the two unknowns at this point takes the form

$$\begin{aligned}
\phi_{\ell-1}(k_1,k_2) + \frac{i}{v_{\alpha_{\ell-1}}} \frac{d\phi_{\ell-1}(k_1,k_2)}{dn} &= 2F_{\ell-1}(k_1,k_2) \\
\phi_{\ell}(k_1,k_2) + \frac{i}{v_{\alpha_{\ell}}} \frac{d\phi_{\ell}(k_1,k_2)}{dn} &= 0 \quad .
\end{aligned} \tag{7f}$$

Then applying the natural boundary conditions

$$\phi_{\ell-1} = \phi_\ell \quad \text{and} \quad \frac{d\phi_{\ell-1}}{dn} = \frac{\rho_{\ell-1}}{\rho_\ell} \frac{d\phi_\ell}{dn} \quad , \tag{7g}$$

equation (7f) reduces to two equations in the two unknowns ϕ_ℓ and $d\phi_\ell/dn$, which immediately yields to the solution:

$$\begin{aligned}
\phi_\ell(k_1,k_2) &= T_{\ell-1,\ell}\, F_{\ell-1} = (1+R_{\ell-1,\ell})\, F_{\ell-1} \\
\frac{d\phi_\ell}{dn}(k_1,k_2) &= i v_{\alpha_\ell} T_{\ell-1,\ell}\, F_{\ell-1}
\end{aligned} \tag{7h}$$

in which

$$R_{\ell-1,\ell} = \frac{v_{\alpha_{\ell-1}}/\rho_{\ell-1} - v_{\alpha_\ell}/\rho_\ell}{v_{\alpha_{\ell-1}}/\rho_{\ell-1} + v_{\alpha_\ell}/\rho_\ell} \quad , \quad T_{\ell-1,\ell} = \frac{2v_{\alpha_{\ell-1}}/\rho_{\ell-1}}{v_{\alpha_{\ell-1}}/\rho_{\ell-1} + v_{\alpha_\ell}/\rho_\ell} \tag{7i}$$

are the plane wave reflection and transmission coefficients at boundary S_ℓ given in terms of ratios of vertical wavenumber divided by density, v_α/ρ_ℓ, for layers ℓ-1 and ℓ, respectively; the vertical wavenumbers, v_α, are in turn given in terms of the wavenumber transform variables (k_1,k_2), the frequency ω and the acoustic velocities $\alpha_{\ell-1}$ and α_ℓ, respectively, as defined in Eq. (7f).

Returning to the system of Kirchhoff integral equations in Eq. (6) for the unknown displacement and traction boundary values, the solution could be calculated directly by solving the system of equations in the wavenumber transform domain to yield

$$\{U,T\} = [I,G_0]^{-1}\{F\} \tag{8}$$

in which the identity and convolutional submatrices have been combined into a square matrix and the unknown displacement and traction boundary values have been combined into a single vector. The inverse matrix operation appearing in Eq. (8) actually reduces to a deconvolutional problem in the wavenumber transform domain; however, the total computational effort is proportional to the number of layers squared. To reduce this squared dependence on the number of layers, the Kirchhoff solution is modified so that only two layers need to be considered at a time leading to a linear dependence on the number of layers.

The reduction to linear cost dependence on the number of layers is made possible by realizing the Eq. (6) is only valid locally or at high frequencies and therefore the coupling from interfaces separated by more than one layer can be ignored without affecting the Kirchhoff solution substantially. To obtain the first order Kirchhoff solution, the direct source field is propagated once through the stack of layers with the boundary interaction considered one interface at a time involving only the propagated field from the previous boundary (or the direct source field for the interface above or below the source) and the boundary values along that interface. If the source is located in the underlying half-space (layer N+1), this gives the upgoing boundary values for the direct arrivals only; conversely if the source is located in layer 1, this gives the direct downgoing boundary values; for sources in intermediate layer ℓ, this gives the direct upgoing boundary values along surfaces $\ell,\ell-1,\ldots,1$ and the direct downgoing boundary values along surfaces $\ell+1,\ell+2,\ldots,N+1$.

Assuming that the source is located in layer ℓ, the direct upgoing boundary values at interface ℓ above the source are found by solving the following pair of equations

$$\begin{aligned} \tfrac{1}{2}\{U_\ell\}_0^u + [\hat{G}^{\ell-1}_{\ell,\ell}]\{T_\ell\}_0^u &= \{0\} \\ \tfrac{1}{2}\{U_\ell\}_0^u + [\hat{G}^{\ell}_{\ell,\ell}]\{T_\ell\}_0^u &= \{F_\ell\} \end{aligned} \qquad (9a)$$

in the wavenumber transform domain at each decoupled sample point analogously to the example in Eqs. (7a) through (7i); if the source is in layer 1, only the second equation is present. The analogous pair of equations for the direct downgoing boundary values at interface ℓ+1 (ℓ=1,2,...,N) are given by

$$\begin{aligned} \tfrac{1}{2}\{U_{\ell+1}\}_0^d + [\hat{G}^{\ell}_{\ell+1,\ell+1}]\{T_{\ell+1}\}_0^d &= \{F_{\ell+1}\} \\ \tfrac{1}{2}\{U_{\ell+1}\}_0^d + [\hat{G}^{\ell+1}_{\ell+1,\ell+1}]\{T_{\ell+1}\}_0^d &= \{0\} \end{aligned} \qquad (9b)$$

.

The vector subscripts 0 in Eqs. (9a) and (9b) represent the zero order Kirchhoff solution and the vector superscripts u and d represent the upgoing and downgoing boundary values, respectively. The zero order (n=0) upgoing boundary values for Eq. (9a) are propagated up to the free surface by solving the following pair of equations in the wavenumber transform domain one interface at a time (i=ℓ-1,ℓ-2,...,2,1):

$$\begin{aligned} \tfrac{1}{2}\{U_i\}_n^u + [\hat{G}^{i}_{i,i}]\{T_i\}_n^u &= \{0\} \\ \tfrac{1}{2}\{U_i\}_n^u + [\hat{G}^{i-1}_{i,i}]\{T_i\}_n^u &= [H^{i+1}_{i,i+1}]\{U_{i+1}\}_n^u - [G^{i+1}_{i,i+1}]\{T_{i+1}\}_n^u \end{aligned} \qquad (10a)$$

For i=1, only the second equation in Eq. (10a) is present and again the displacements equal twice the upgoing field. In all cases, the right-hand side of Eq. (10a) is known from the solution at the previous interface. The analogous pair of equations for the zero order (n=0) downgoing boundary values for successive interfaces i=ℓ+2, ℓ+3,...,N+1 (ℓ<N):

$$\begin{aligned}\frac{1}{2}\{U_i\}_n^d + [\hat{G}^{i-1}_{i,i}]\{T_i\}_n^d &= [H^{i-1}_{i,i-1}]\{U_{i-1}\}_n^d - [G^{i-1}_{i,i-1}]\{T_{i-1}\}_n^d \\ \frac{1}{2}\{U_i\}_n^d + [\hat{G}^{i}_{i,i}]\{T_i\}_n^d &= \{0\}\end{aligned} \qquad (10b)$$

At this stage, the upgoing and downgoing boundary values have been calculated and stored at all sample points for the zero order (n=0) solution, which represents the direct arrivals from the source (no higher order multiple reflections). If higher order multiples are desired, the recursive cascading process is performed. The next order solution (n) is obtained by reversing the propagation direction from the previous pass through the layers. The downgoing boundary values from interface N+1 in Eq. (10b) are used in the right-hand side of Eq. (10a) for i=N and the upgoing boundary values are calculated interface by interface (i=N,N-1,...2,1) for the next order reflection and added to any previously calculated upgoing boundary values. Analogously, the upgoing boundary values from interface 1 in Eq. (10a) are used in the right-hand side of Eq. (10b) for i=2 and the downgoing boundary values are calculated interface by interface (i=2,3,...,N,N+1) for this next order reflection and added to any previously calculated downgoing boundary values.

Note for the first order (n=1) reflections only, the direct arrival terms (n=0) are zero for the upgoing boundary values along surfaces below the source (ℓ+1,ℓ+2,...,N) and for the downgoing boundary values along surfaces above the source (ℓ,ℓ-1,...,1).

After the cascading process is complete up to the desired reflection order, the total boundary values for the modified Kirchhoff solution are obtained by adding the upgoing and downgoing boundary values along each interface, i=1,2,...,N+1:

$$\begin{aligned}\{U_i\} &= \{U_i\}_n^u + \{U_i\}_n^d \\ \{T_i\} &= \{T_i\}_n^u + \{T_i\}_n^d\end{aligned} \qquad (11)$$

Then the displacement field at any additional locations within any layer is obtained at this frequency by introducing the boundary values from Eq. (11) into the representation theorem of Eq. (1). Time domain results, if desired, would be obtained through Fourier synthesis by calculating modified the Kirchhoff solution at a discrete set of frequency values.

Alternatively, one can formulate the Kirchhoff solution directly in the time domain using time domain analogs of the full-space frequency domain Green's functions given in Appendix A to perform the propagation between boundaries. The boundary interaction at a local point on surface S_ℓ is accomplished by performing a plane wave decomposition of the incoming wave field in the local tangent plane coordinates. The effective angle of incidence of the equivalent incoming plane wave at a local boundary point is determined from the following plane wave identity in the local tangent plane coordinates

$$d\phi_\ell/dn = - i\omega v_\ell d\phi_\ell/dt$$

by solving for the vertical wavenumber v_ℓ (i.e., cosine of angle of emergence divided by velocity) at each time point. This permits pointwise application of the reflection and transmission coefficients to the equivalent incoming wave field from an adjacent boundary, reducing spurious arrivals from integration points beyond critical angle.

3.2 Results

A time domain Kirchhoff algorithm has been developed using the methodology outlined in Section 3.1 and has been tested and applied to a number of interesting geologic models. The algorithm is quite general, allowing for three-dimensional multilayered elastic model specifications. The limitations on the model input include a requirement that the minimum distance between two boundaries be greater than the surface sampling distance and a precaution that the results become unreliable for steeply dipping structures or any other situation involving multiple interactions of the wavefield with the boundary. A direct comparison is made in Section 4.2 between the Kirchhoff solution and the more rigorous iterative BIE solution, graphically displaying some of these deficiencies. The Kirchhoff algorithm performs all its operations for fully 3-D models. However, the demonstrational applications presented in this section involve models with constant material properties perpendicular to the vertical 2-D plane defining the layer properties.

In the first application, the Kirchhoff algorithm was used to show the near-source structural effects on body waves in the vicinity of Yucca Flats at the Nevada Test Site (Mellman, et al., 1982). The simulated results were shown to reproduce the gross features observed in waveform variation and amplitude variation across the northern portion of the basin, solely by modeling the interference effects from the layer discontinuity along the Cenozoic-Paleozoic basement contact. In the southern portion of the basin, however, the steeply dipping sidewalls cast some doubts on the reliability of the Kirchhoff results and the comparisons between synthetics and observations were less satisfactory.

A contour map of the depth to the Paleozoic contact at Yucca Flats has been determined by Herrin and Goforth (1981) as shown in Figure 2. The line A-A' is chosen to be perpendicular to the major axis of the basin, in a region which is essentially two-dimensional in nature. This allows for results obtained on line A-A' to be applied to nearby source locations with some degree of confidence. A cross-section view, along line A-A', of the model is shown in Figure 3. Squares represent grid points, while the normals to the surface at each grid point designated by a short line segment at each grid point. Note that irregular grid spacing has been deployed to provide improved accuracy and efficiency. Source locations are chosen along line A-A' and are uniformly spaced at a depth of 550 meters as shown on the artificial intermediate layer boundary with source locations numbered from west to east. The sides of the basin are tapered at a depth of 200 meters to prevent numerical instabilities associated with boundaries being too close. The material properties in the tuff layer represent an average of saturated and unsaturated values, because the water table interface occurring at a constant depth of about 500 meters was removed from the model to

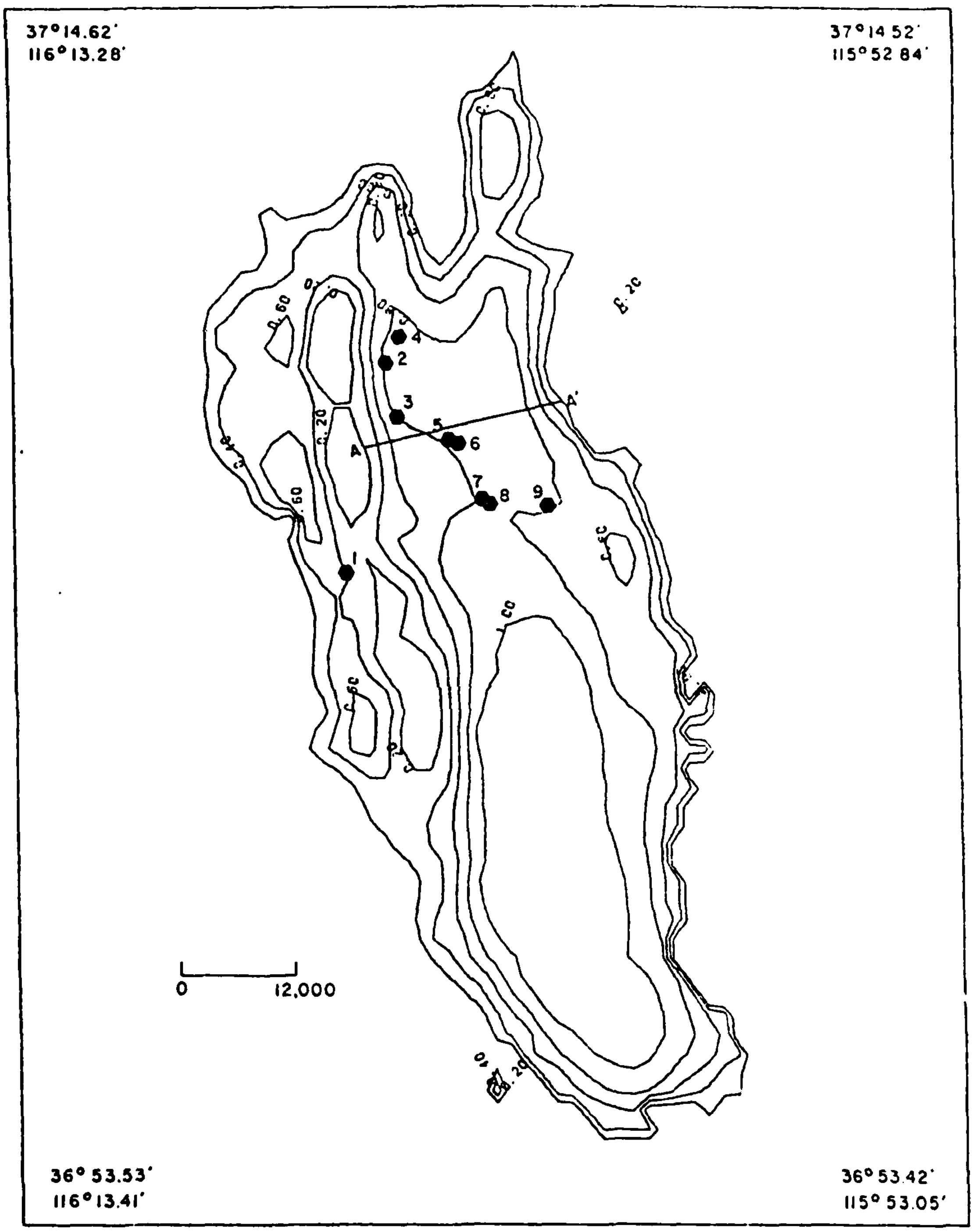
37°14.62'
116°13.28'
37°14.52'
115°52.84'
0.60
0.20
.60
A
A'
1
2
3
4
5
6
7
8
9
0
12,000
36°53.53'
116°13.41'
36°53.42'
115°53.05'

Figure 2. Contour map of Cenezoic-Paleozoic contact for Yucca Flats are determined by Herrin et al. Line A-A' corresponds to cross section shown in modeling plots. Locations 1-9 are selected events used in waveform comparisons.

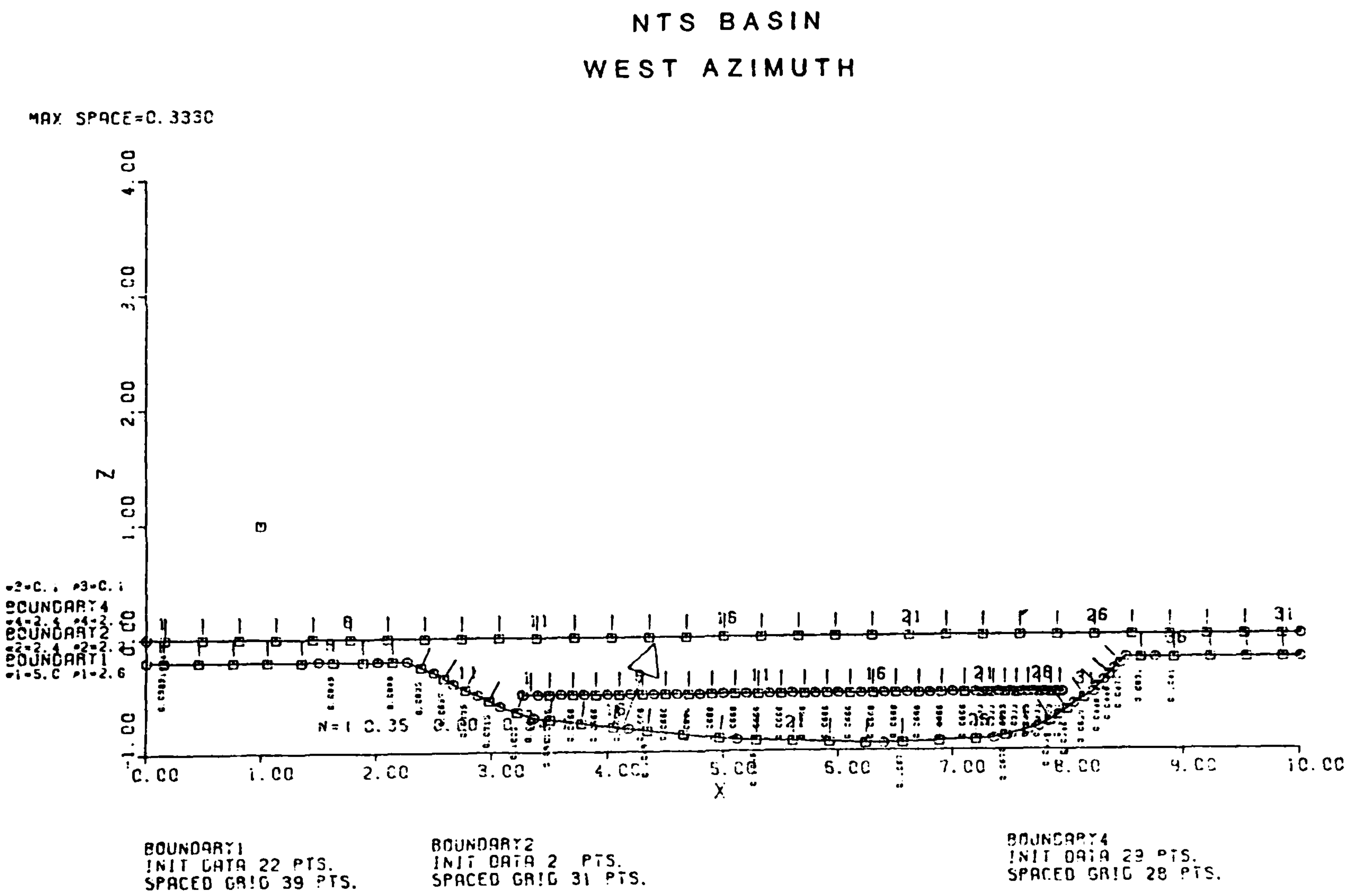

Figure 3. Cross section A-A' and grid for northern basin model, showing surface, Cenezoic-Paleozoic boundary and source locations. Arrow indicates direction of propagation of plane wave in reciprocal problem.

accommodate the basin tapering. The P and S wave velocities and density in the tuff layer are accordingly set to 2.4 km/sec, 1.4 km/sec and 2.2 gm/cm^3, respectively, and the corresponding values in the Paleozoic zone are 4.8 km/sec, 2.8 km/sec and 2.6 gm/cm^3.

Reciprocity arguments are involved such that incident planes waves with ray parameter of .07 sec/km provide synthetic seismograms at teleseismic receiver distances of about 60 degress due to the source locations displayed along line A-A' of Figure 3. The synthetic seismograms are shown in Figures 4, 5 and 6 for receivers located in azimuths west, north and east of the basin, respectively. In each case, the response at the far field station is displayed due to every fifth source location on line A-A'. The time series correspond to realistic explosion source seismograms because the impulse response Kirchhoff solution has been convolved with a von Seggern and Blandford (1972) time function characterized by k=10 and B=2, an attenuation operator (Futterman, 1966) characterized by t*=.6, a typical receiver function (Lundquist and Kam, 1982) and a KS instrument response. In all cases reflections of up to order two have been included by making three passes through the layers.

The large, early arriving reflection from source 1 interferes constructively with the multiple reflections from the western portion of the basin in Figure 4, giving rise to the focussed (narrow) first trough and second peak in the waveform. The greater delay of this reflection off the bottom and side of the basin for sources located closer to the center of the basin (eg., sources 11 and 16) results in defocussing (broadening) of the waveform, an attendant decrease in amplitude, and the development of an inflection in the second peak. Near the eastern portion of the basin (eg., sources 21 and 26), there is an increase in amplitude and decrease in pulse width due to the proximity of the eastern wall. The corresponding synthetic seismograms for the northern and eastern azimuths are shown in Figures 5 and 6. In general there is a somewhat reduced amplitude and waveform variation in these azimuths as a function of source location across the basin. The predicted amplitude and waveform variations in all three azimuths are

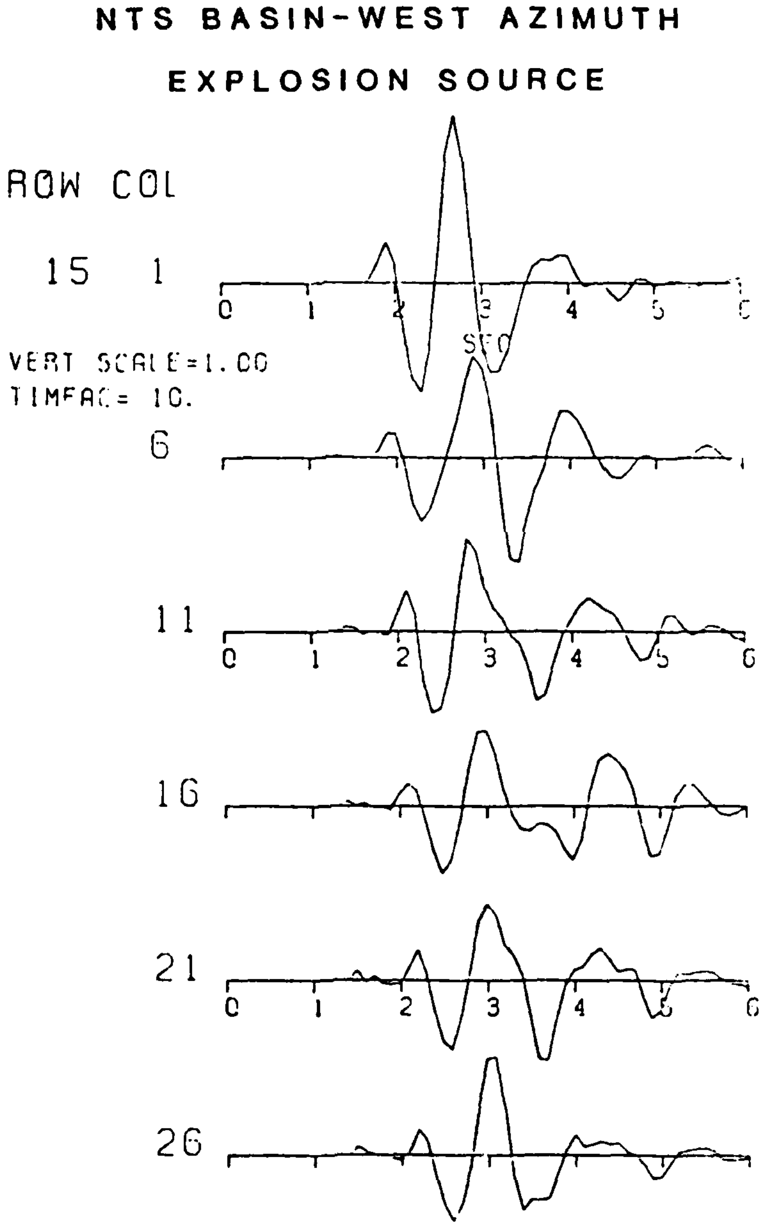

Figure 4. Synthetic seismograms in the Western azimuth for model in Figure 3 using SRO instrument, von Seggern-Blandford source function with k=10, B=2, receiver function for station E from E. Kazakh events and additional attenuation operator with t*=.6 seconds.

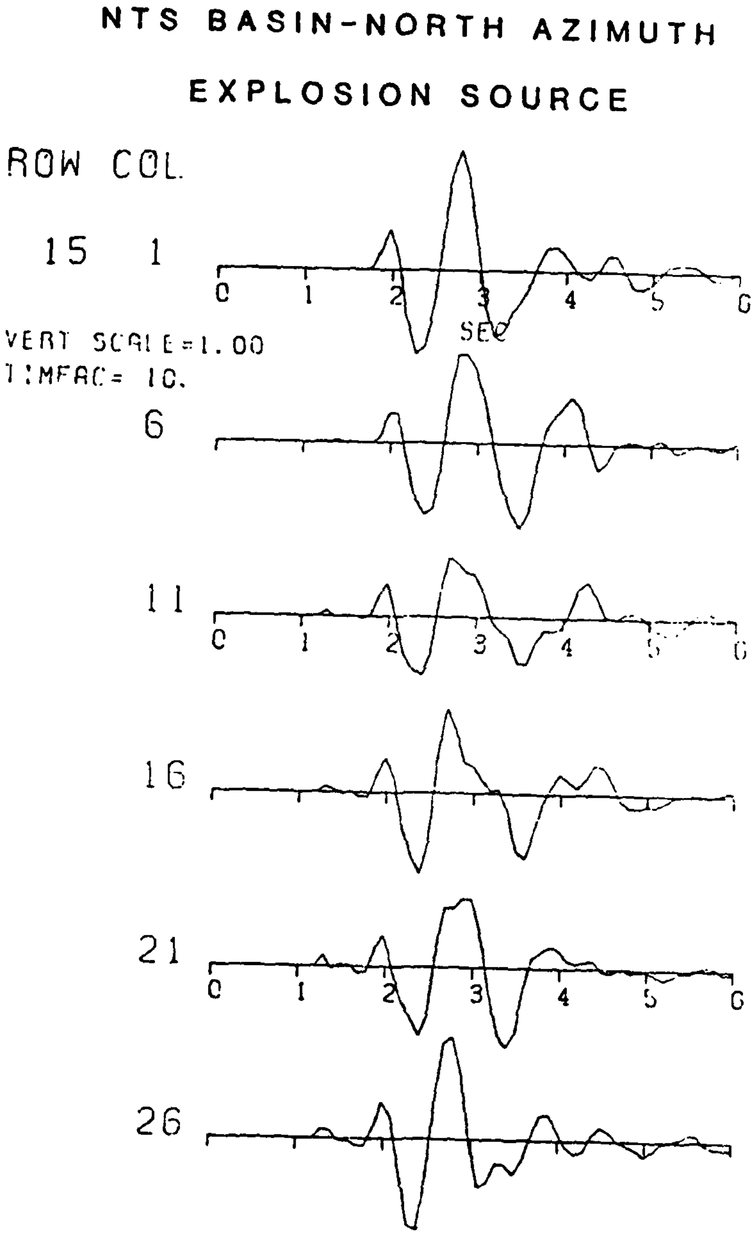

Figure 5. Synthetic seismograms, as in Figure 4 but the North azimuth.

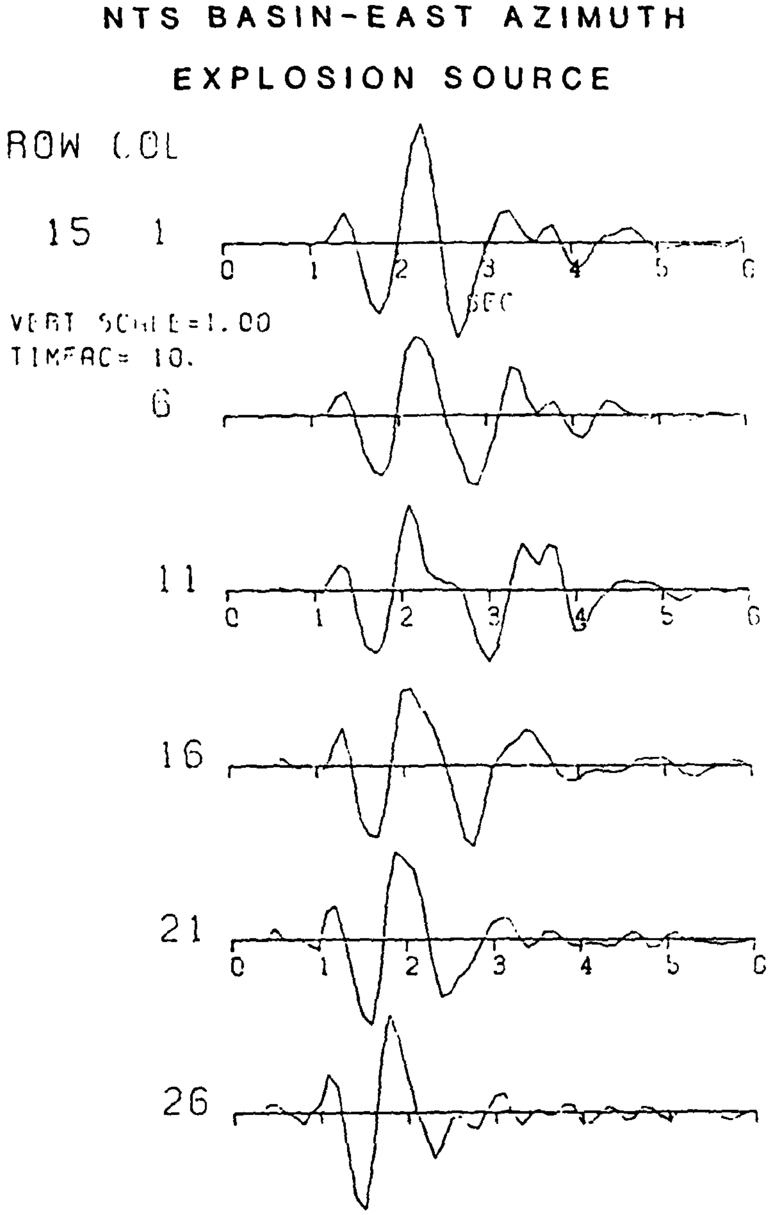

Figure 6. Synthetic seismograms, as in Figure 4 but for East azimuth.

consistent with observations from the nine underground nuclear explosions located near line A-A' (refer to Figure 2 for the locations and to Mellman, et al., 1982, for the comparisons between observations and synthetics). The synthetic seismograms located in a southern azimuth (not shown) were found to be less satisfactory in reproducing the general trends in the observations in that region. This is presumably due to the presence of extreme dips in the near-source structure of that area, which is not properly handled with the Kirchhoff solution technique. The Kirchhoff code proved instrumental in relating the observed amplitude and waveform variations at Yucca Flats to interference effects of known shallow structure rather than to focussing caused by deeper structure.

In a similar study, the effects of basins on earthquake strong ground motions were investigated using the Kirchhoff algorithm (Hadley, 1982). Figure 7 shows an example calculation for a simple basin model with the earthquake source located beneath the basin. The incident energy is from the right side of the basin, propagating parallel to the indicated arrow. The P-wave velocity in the layer is 2 km/sec and the basement velocity is 4 km/sec. As in the Yucca Flats study, the calculations include two internal multiple reflections within the structure. The absolute levels of motion and variability of ground shaking caused by the basin structure are evidenced in the displayed synthetic seismograms superimposed at seven receiver locations across the basin. Note the long duration and large amplitudes of the simulated records along the left half of the basin in the direction of the incoming energy. Amplifications by the basin structure caused by focusing is responsible for the amplitude variations of about a factor of three.

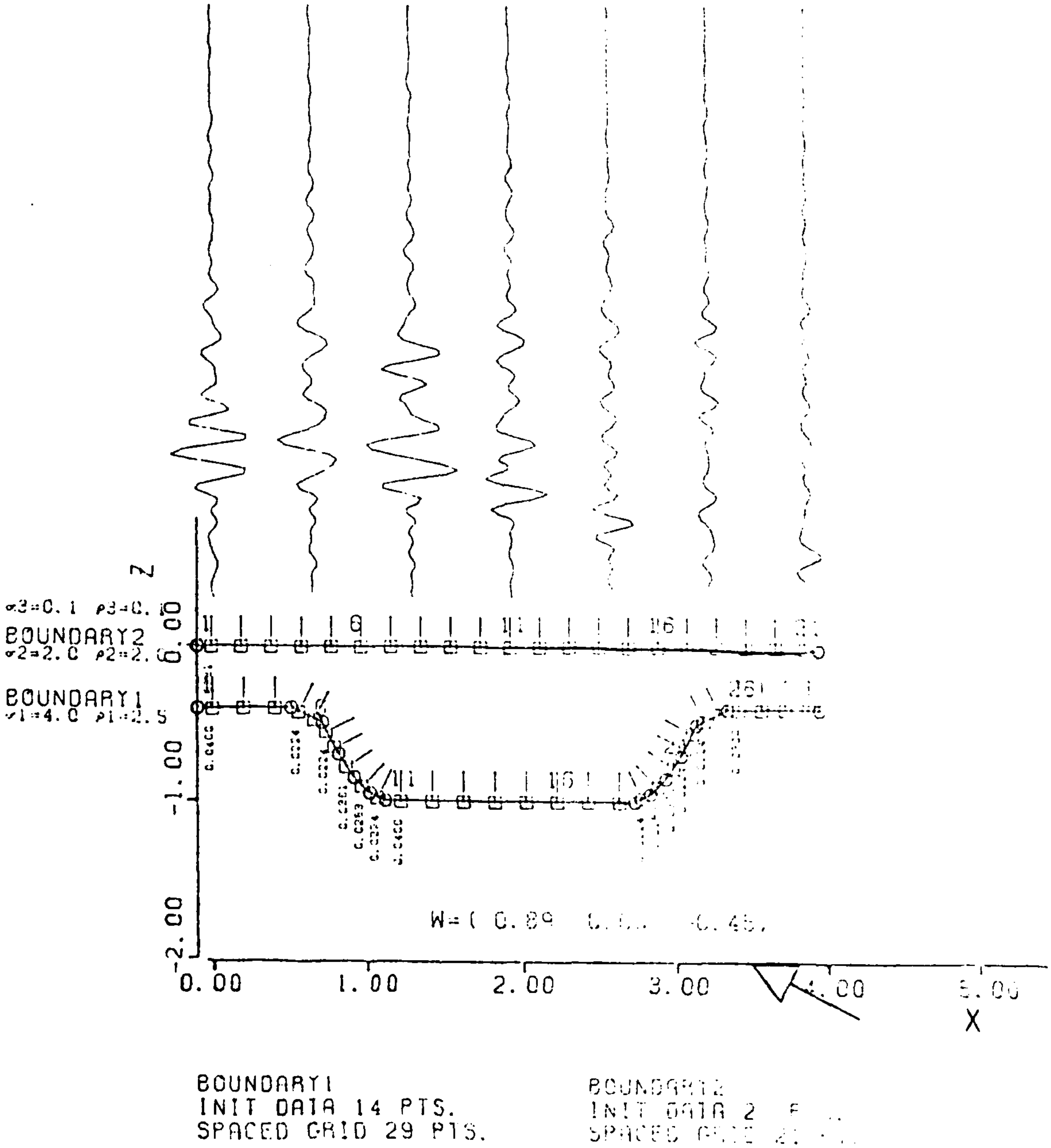

Figure 7. Waveforms and relative amplitudes for a wave incident at a shallow angle from the right (arrow). The synthetic time histories have been calculated with the Kirchhoff technique and includes two multiples within the basin. Note the factor of 3 increase in amplitude caused by structure.

4. SOLUTION USING RIGOROUS ITERATIVE BIE APPROACH

In this chapter, a rigorous iterative approach is used to solve the general BIE problem formulated in Chapter 2. The solution technique is described in Section 4.1. Included is a discussion of how the singularities are handled in the general formulation which leads to an iterative treatment based on perturbing the model from a flat layer point of view. The matrix equation becomes well conditioned and numerically tractable after the singularities have been removed and all matrix inversion operations are reduced to simpler deconvolutional operations by virtue of the iterative solution approach. The solution provides kinematic and dynamic effects equally accurately at low and high frequencies and handles incident waves beyond critical angle and even layer pinchouts.

Sample applications are presented in Section 4.2 for the simple cases of waves impinging on an irregular free-surface of a semi-infinite half-space and transmission through an irregular interface for a single layer overlying a semi-infinite half-space. The convergence of the BIE solution is demonstrated and comparisons are shown with the approximate Kirchhoff solution. The deficiencies of the Kirchhoff approximation are easily identified from these simple models and the zero order iteration is shown to provide results more accurate than the approximate Kirchhoff solution. Applications to more complicated models are discussed in Chapter 5.

4.1 Methodology

In the iterative frequency domain treatment of the general BIE problem presented in Chapter 2, the interaction of the propagating wavefield with the boundaries is satisfied globally including rigorous interaction between neighboring points on a single boundary. The first step in deriving the iterative BIE solution is to remove the singularities from the Green's functions in Eq. (5). These singularities occur when a quadrature point along boundary ℓ coincides with a sample point along boundary ℓ and are evidenced along the diagonal elements of sub-matrices $[G^{n}_{\ell\ell}]$ and $[H^{n}_{\ell,\ell}]$ for $\ell=2,3,\ldots,N+1$ and $n=\ell-1,\ell$ (eg., when sample point $\vec{x}_\ell$ coincides with quadrature point $\vec{y}_\ell$ in the second integral of Eq. (4a) and the first integral of Eqs. (2) and (4b)). This is typically the case in the general BIE formulation because it is desirable to be able to use the same sample points as quadrature points in propagating the boundary values from interface ℓ to interfaces ℓ-1 and ℓ+1. Singularities can also occur when two interfaces pinchout so that a quadrature point on an adjacent boundary (ℓ+1 or ℓ-1) coincides with a sample point along boundary ℓ. If pinchouts exist in the model, these singularities would be evidenced in certain elements of submatrices $[G^n_{\ell+1,\ell}]$ and $[H^n_{\ell+1,\ell}]$ or $[G^n_{\ell-1,\ell}]$ and $[H^n_{\ell-1,\ell}]$ (eg., when sample point $\vec{x}_\ell$ coincides with quadrature points $\vec{y}_{\ell+1}$ or $\vec{y}_{\ell-1}$ in the first integral of Eq. (4a) or in the second integral of Eqs. (2) or (4b), depending on which two layers are pinching out). Even if the sample points were slightly offset from the quadrature points, the matrix would still be too ill-conditioned to be numerically tractable.

Basically there are three techniques for dealing with these singularities with various degrees of generality and effectiveness. One method would be to deal with the singularities directly by invoking various smoothness criteria and taking principal values. This has the distinct disadvantages of reducing flexibility in the formulation and of being unstable and inefficient during applications. A second method would be to express the unknown displacement and traction boundary values in terms of integral representations of unknown forces located on deformed surfaces interior to the actual bounding surfaces and then to solve for the set of unknown forces that simultaneously satisfies all the boundary and continuity conditions (see, for example, Ohsaki, 1973 and Part II of Apsel, 1979). In general, this treatment is quite effective because the singularities are avoided altogether except for layer pinchouts (or very thin layers) because some quadrature points on the deformed surface would still coincide some of the sample points (or be so close that the system of equations becomes ill-conditioned). If it weren't for the possibility of layer pinchouts, the equivalent force treatment would be useful because of the simpler formulation and the elimination of the need to evaluate and deal with the spatial derivatives of the stress Green's function components in the traction integral representations.

The third method, which is the preferred choice, involves analytically subtracting off the singularities from the Green's functions using the flat layer Green's functions and iteratively solving the complete BIE problem with the flat layer solution as a starting solution on the first iteration. This has the distinct advantages of removing the singularities under all situations, properly conditioning the dense BIE matrix and replacing the matrix inversion operations involving the dense BIE matrix with simple deconvolution operations that are handled quite efficiently using Fourier transform techniques.

Another important advantage of using this approach to remove the singularities is the simple provision for dealing with potentially spurious edge effects arising from the necessarily finite horizontal extremes of the model when carrying out the successive iterations on the solution. For layer boundaries converging to the depth of the artificial flat layer, the integrals along those extremities go identically to zero by virtue of the perturbation formulation. For those boundaries converging to a constant depth different than that of the flat layer, the first order edge effects are still removed leaving higher order effects governed by the ratio of the horizontal distance from sample point to quadrature point divided by the vertical offset from the flat layer (indicating that the higher order edge effects can be removed either by integrating along this extremity until the offset ratio is sufficiently small or by tapering the diminishing Green's function perturbations). For those boundaries deviating from the artificial flat layer at the extremities of the model, tapering will be necessary on the nonvanishing Green's function perturbations unless the model can be extended until the layer boundaries eventually approach zero dip. For the zero order iteration, tapering will typically be required at the extremities of the artificial flat boundaries to obtain the flat layer solution (unless geometrical spreading or material attenuation behavior are sufficient to truncate the integrals without tapering). In any case, it is quite straightforward to avoid spurious edge effects in Sierra Geophysics' iterative BIE solution. This is in direct contrast to finite difference of finite element techniques or other BIE solution techniques where either appropriate nonreflecting boundary conditions must be used (such as in Scheuster's

(1983) BIE solution) or else the model grid must be extended far beyond the region of interest (such as in Cole's (1980) time domain BIE solution) so that the spurious edge reflections arrive sufficiently late not to contaminate the signal of interest.

The iterative solution technique at a given frequency for the general BIE formulation in Eq. (5) is derived by first subtracting off the singularities. This is effectively accomplished by reformulating the general BIE problem in terms of a perturbation problem with respect to flat layers. The matrix equation for the flat layer problem in which the flat layers are passed through the reference planes of the original irregular layers is written as

$$[I]\{U_o\} = [H_o]\{U_o\} - [G_o]\{T_o\} + \{F_o\} \tag{12}$$

in which $\{U_o\}$, $\{T_o\}$, $\{F_o\}$, $[G_o]$ and $[H_o]$ have the analogous definitions as in Eq. (5) for the flat layer problem instead of the *irregular layered problem. In the limit as sample point and quadrature* point coincide, the singular elements of $[G_o]$ and $[H_o]$ exactly approach the singular elements of [G] and [H], respectively. Therefore, if the original BIE problem could be recast in terms of the perturbation matrices $[G-G_o]$ and $[H-H_o]$, formed by analytically subtracting the nontrivial elements of $[G_o]$ and $[H_o]$ from the corresponding elements of [G] and [H], then all singularities would be automatically handled.

As an example, consider the form of the singularities arising from interaction of the wavefield with a boundary in 2-D acoustic structures. The horizontal sample position on the irregular boundary is defined by the coordinates (x,z), with z being a function of x. The artificial flat layer is defined at a constant depth of $z = z_o$ and integration is carried out along the boundary over all quadrature points x_o. The singularity arises in the imaginary part of the Hankel functions of order zero and one when quadrature point x_o approaches sample point x in [G]. Then, when the perturbation matrix $[G-G_o]$ and $[H-H_o]$ are formed, the difference of the imaginary parts of the singular elements (irregular operator minus flat operator) has the following form including the quadrature coefficients:

$$\{ Y_m[k\sqrt{(x-x_o)^2+(z-z_o)^2}]\sqrt{1+(dz/dx)^2} - Y_m[k|x-x_o|] \} dx_o \quad , \quad (m=0,1) \qquad (13)$$

in which $Y_m(r)$ is the Bessel function of the second kind of order m and k is the horizontal wavenumber equal to frequency divided by acoustic velocity. Using the fact that $Y_0(r) \sim (2/\pi) \ln(r)$ and that $Y_1(r) \sim -(2/\pi)/r$ in the limit as r goes to zero, it is straightforward to prove (using l'Hôspital's Rule) that the difference of the two terms in Eq. (13) is identically zero in the limit as x approaches x_o. The entire row of terms appearing in matrices $[G-G_o]$ and $[H-H_o]$ for other values of x_o in Eq. (13) are in fact better conditioned. The behavior at the extremities of the boundary is also evident from Eq. (13). For irregular boundaries converging to the artificial flat layer, coordinate z approaches the constant z_o and the difference in Eq. (13) is identically zero; for boundaries converging to a different constant depth, z_1, the difference approaches zero as the absolute value of the ratio $(x-x_o)/(z_1-z_o)$ increases.

The iterative BIE solution technique proceeds by rewriting Eq. (5) without change by adding and subtracting the flat layer terms:

$$[I]\{\tilde{U}+U_o\} = [\tilde{H}+H_o]\{\tilde{U}+U_o\} - [\tilde{G}+G_o]\{\tilde{T}+T_o\} + \{\tilde{F}+F_o\} \qquad (14)$$

in which

$$\{\tilde{U}\} = \{U-U_o\} \ , \ \{\tilde{T}\} = \{T-T_o\} \qquad (15)$$

are the unknown perturbed displacement and traction boundary value vectors, respectively;

$$[\tilde{G}] = [G-G_o], \ [\tilde{H}] = [H-H_o] \qquad (16)$$

are the perturbed displacement and traction Green's function matrices; and

$$\{\tilde{F}\} = \{F-F_o\} \tag{17}$$

is the perturbed direct source field vector. Eq. (12) is then used directly to simplify Eq. (14), which after rearranging, takes the form

$$[I]\{\tilde{U}\} - [H_o]\{\tilde{U}\} + [G_o]\{\tilde{T}\} = [\tilde{H}]\{\tilde{U}+U_o\} - [\tilde{G}]\{\tilde{T}+T_o\} + \{\tilde{F}\}, \tag{18}$$

in which all matrices are nonsingular and well behaved: matrix $[I]$ consists of identity and null submatrices; the rows of matrices $[G_o]$ and $[H_o]$ are convolutional operators on vectors $\{\tilde{T}\}$ and $\{\tilde{U}\}$ for constant material properties in each layer; and the rows of matrices $[\tilde{H}]$ and $[\tilde{G}]$ are small and smoothly varying for structures not deviating too widely from the reference flat layers.

Next, Eq. (18) is rewritten using more compact ontation:

$$[C]\{\tilde{X}\} = [\tilde{A}]\{\tilde{X}+X_o\} + \{\tilde{F}\} \tag{19}$$

in which vector $\{\tilde{X}\}$ contains all the unknown perturbed boundary values along all layer boundaries:

$$\tilde{X} = \{\tilde{U}_1\},\{\tilde{U}_2\},\{\tilde{T}_2\},\{\tilde{U}_3\},\{\tilde{T}_3\}, \ldots,\{\tilde{U}_{N+1}\},\{\tilde{T}_{N+1}\} \tag{20}$$

where subvectors $\{\tilde{U}_\ell\}$ contains the $3q_\ell$ unknown perturbed displacement boundary values $(u-u_o)$ along interface ℓ $(\ell=1,2,\ldots,N+1)$ and subvectors $\{\tilde{T}_\ell\}$ contain the $3q_\ell$ unknown perturbed traction boundary values $(T-T_o)$ along interface ℓ $(\ell=2,3,\ldots,N+1)$. Vector $\{X_o\}$ is defined analogously to Eq. (20) for the flat layer displacement and traction boundary values, so that the actual boundary values are given by

$$\{X\} = \{\tilde{X}\} + \{X_o\}. \tag{21}$$

The square matric $[\tilde{A}]$ contains the relatively small and well behaved submatrices from $[\tilde{H}]$ and $[\tilde{G}]$. The square matrix [C] contains the identity submatrices from [I] and the convolutional submatrices from $[G_o]$ and $[H_o]$. Therewith Eq. (19) can be written in its final form, which is ideally suited for an iterative solution approach:

$$\{\tilde{X}\}_n = \{\tilde{X}\}_0 + [P]\{\tilde{X}_{n-1} + X_o\} \quad , n = 1,2,... \tag{22}$$

in which the zero order iterative solution $\{\tilde{X}\}_0$ is given by

$$\{\tilde{X}\}_0 = [C]^{-1}\{\tilde{F}\} \qquad ; \tag{23a}$$

the flat layer solution $\{X_o\}$ is given by

$$\{X_o\} = [C]^{-1}\{F_o\} \qquad ; \tag{23b}$$

and the recursive matrix operator [P] is given by

$$[P] = [C]^{-1}[\tilde{A}]. \tag{23c}$$

Note that $\{\tilde{X}\}_0$, $\{X_o\}$ and [P] are all independent of iteration number n and are efficiently calculated all at once in the Fourier transform domain as the inverse operation involving matrix [C] decouples into a simpler deconvolutional problem.

The nth iteration estimates to the perturbed boundary values are obtained by recycling the values from iteration number n-1 through the right-hand side of Eq. (22) to obtain an improved solution to the unknown perturbed boundary values. The recursive process in Eq. (22) is numerically stable and convergent. The convergence proof would require a detailed discussion of the norm of matrix [P] in Eq. (23c) and will not be presented here. However, in all cases where the technique has been applied, the successive iterations have exhibited convergent behavior. As the number n of successive iterations is increased, the amount of high order interaction of the wavefield with the boundaries is also increased. Also, the zero order iteration is often considerably more accurate than the approximate Kirchhoff solution of the previous chapter and is useful in itself.

Once the desired number of iterations has been carried out, the final solution for the unperturbed boundary values is obtained from Eq. (21) in which the final solution to the perturbed boundary values $\{\tilde{X}\}$ is given by the nth order iteration in Eq. (22) and the flat layer solution $\{X_0\}$ is given by Eq. (23b). Then, analogous to the final propagation step in the Kirchhoff solution technique, the displacement field at any additional locations within any layer is obtained at this frequency by introducing the boundary values from Eq. (21) into the representation theorem of Eq. (1). Time domain results, if desired, would be obtained through Fourier synthesis by calculating the iterative BIE solution at a discrete set of frequency values.

4.2 Results

An iterative frequency domain BIE algorithm has been developed for treating three simple cases using the methodology outlined in Section 4.1. The three cases include the following two-dimensional acoustic problems: (1) wave propagation in a semi-infinite space with an irregular free surface; (2) wave propagation through an irregular interface in an infinite space; and (3) wave propagation in a layer overlying a semi-infinite space with an irregular interface and a flat free surface. The results for these simple cases illustrate the effectiveness of the iterative BIE technique and are presented in this section. Extensions to a more general iterative BIE algorithm are discussed in Chapter 5.

A comparison between the Kirchhoff solution (from Section 3.1) and the iterative BIE solution (from Section 4.1) is presented in Figures 8 and 9 for the case of a plane monochromatic wave in a semi-infinite space normally incident to an irregular free surface with a simple bump. The power density of the scattered field is shown in Figure 8 at a frequency corresponding to a horizontal wavenumber (ω/α) of 1.5 for the half-space. The Kirchhoff solution is shown in the upper left plot with the zero order, first order and successive iterations of the BIE solution shown in the center left, lower left and right-column plots, respectively. In each of the six plots, the response is shown as a function of increasing horizontal position and increasing vertical depth into the half-space with the amplitudes color scaled between dark red for the maximum value through yellow, green and light blue for the intermediate values, down to dark blue for the minimum value (zero for the power density plots). It is seen that the Kirchhoff solution fails to reproduce the diffractive effects arising along the incline of the surface bump. By the second iteration of the iterative BIE soluton, these diffractive effects are nicely produced and convergence is verified by comparison to the third and fourth iteration plots. Even the zero order BIE solution is considerably more accurate than the Kirchhoff solution.

The corresponding time domain comparisons are shown in Figure 9. For the time domain plots, the vertical axis represents the horizontal receiver positions as a function of increasing distance along a flat line several grid dimensions below the reference plane of the irregular free surface. The color coding convention is the same as in Figure 8 with red being the most positive (at the focus of scattered energy) and dark blue being the most negative (along the reflected power plane wave). The response has been convolved with a Gaussian-shaped wavelet. The largest deficiencies evidenced in the Kirchhoff solution in the upper left plot are the inaccurate amplitudes and inaccurate travel-time delays for the later diffractive arrivals, substantiating the indicated deficiencies at the particular frequency used in Figure 8. The excellent convergence of the BIE solution in the time domain verifies that the technique works equally well at low and high frequency. Also, there are no edge

Figure 8. Comparison of the power density of the scattered field due to a vertically incident plane wave impinging on the free surface with a bump between the Kirchhoff solution and the various iterations of the more rigorous BIE solution. All plots are scaled to absolute range (0.1, 3.0).

Best
Available
Copy

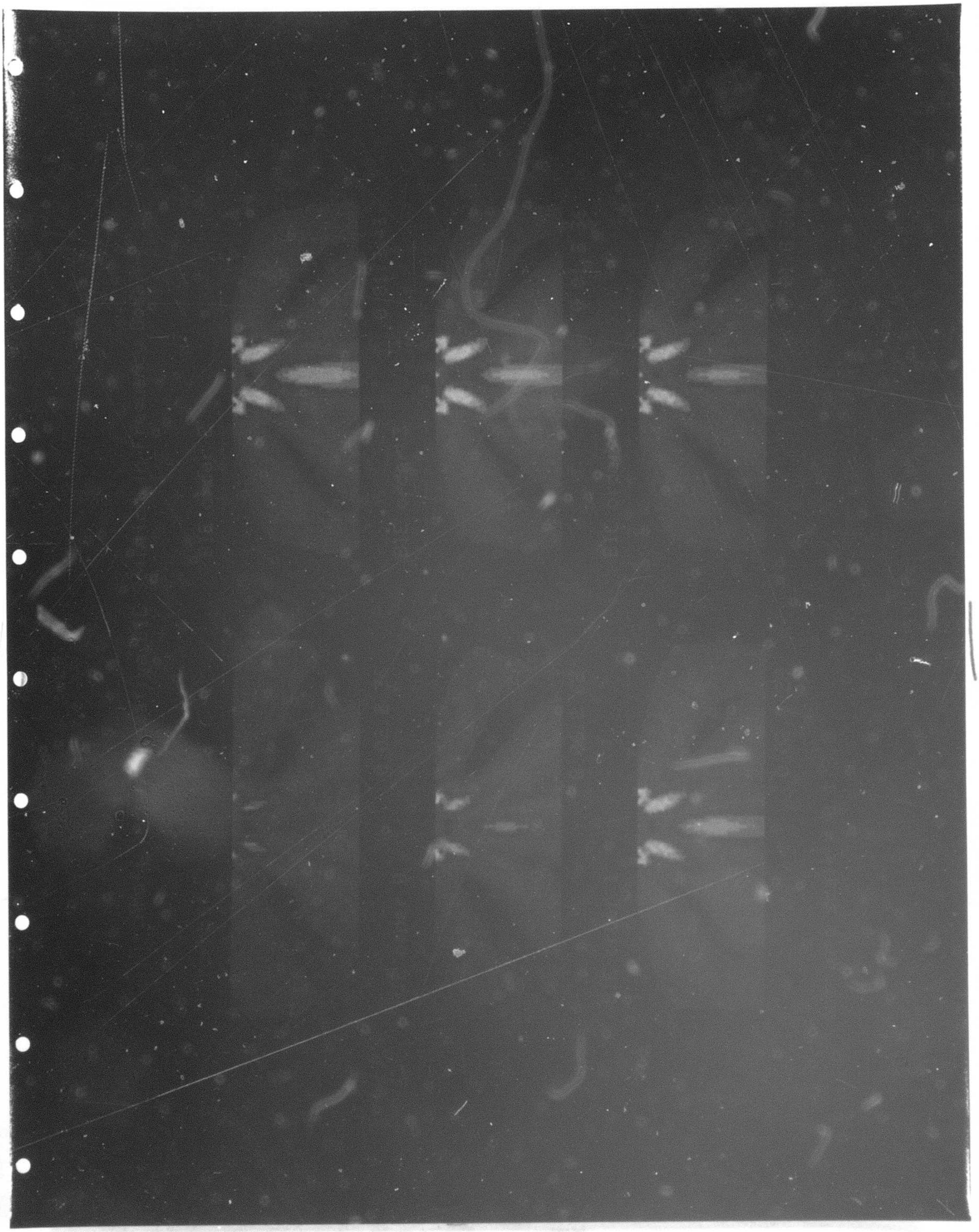

Figure 9. Corresponding comparison to Figure 8 in the time domain between the Kirchhoff solution and the iterative BIE solutions along a line of receivers located several grid dimensions below the free surface. All plots are scaled to absolute range (-1.0, 0.5).

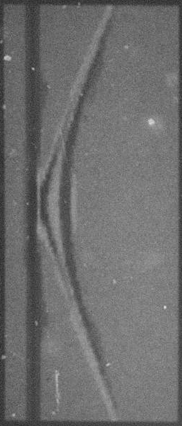
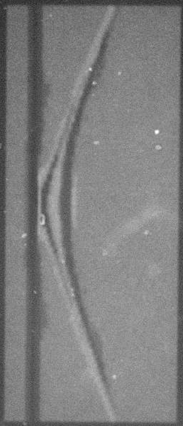
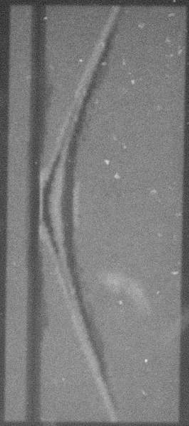
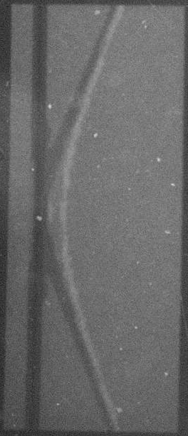
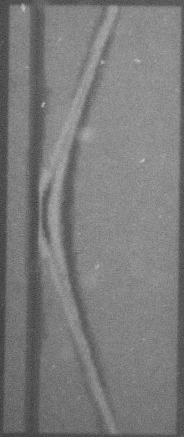
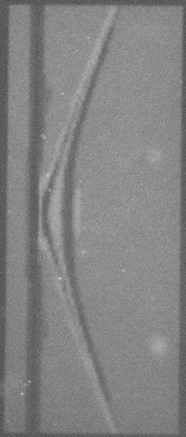

reflections contaminating the signal verifying that the technique effectively avoids these spurious arrivals. Again, even the zero order BIE solution is considerably more accurate than the Kirchhoff solution.

The next three figures show the sensitivity of the iterated BIE solution to various model parameters for the case of a simple bump on the free surface of a half-space. In Figure 10, the power density of the scattered field due to a normally incident plane wave is compared at six frequencies from low frequency (upper left plot with k=0.1) to high frequency (lower right plot with k=2.1) with each plot self-scaled. The most obvious trend to notice in these six plots is the increasingly focussed reflections and diffractions from the surface bumps as the frequency is increased. At low frequency, the wavelength is approaching or exceeding the dimensions of the surface bump, reducing the diffractive effects and causing the bump to act like a point source emitter. In Figures 11 and 12, the iterated BIE solution due to a normally incident plane wave is compared for different size surface bumps in the frequency domain and time domain, respectively. The power density of the scattered field at an intermediate frequency corresponding to k=1.5 is shown for no bump in the upper left hand plot to the largest bump in the lower right hand plot, with all plots displayed using the same absolute color scaling. As expected, there is no scattered field for the flat free surface with increasingly larger scattered energy and larger dispersion of diffractive energy as the bump is increased in size. The analogous results in the time domain including the reflected wave are shown in Figure 12 for a line of receivers located several grid dimensions below the free surface. All six plots are displayed using the same absolute color scaling with the most negative arrivals (dark blue) corresponding to the reflected plane wave and the most positive arrivals (red) corresponding to the maximum scattered field.

The next four figures show the sensitivity of the iterated BIE solution to various model parameters for a more arbitrary irregular free surface. In Figures 13 and 14, the scattered power density field is shown for vertically incident and obliquely incident (30 degrees from vertical) plane waves, respectively. In both figures, the field is compared at

Figure 10. Power density of the scattered field due to a vertically incident plane wave impinging on a free surface with a bump calculated with the iterative BIE technique at six different frequencies. All plots are self-scaled.

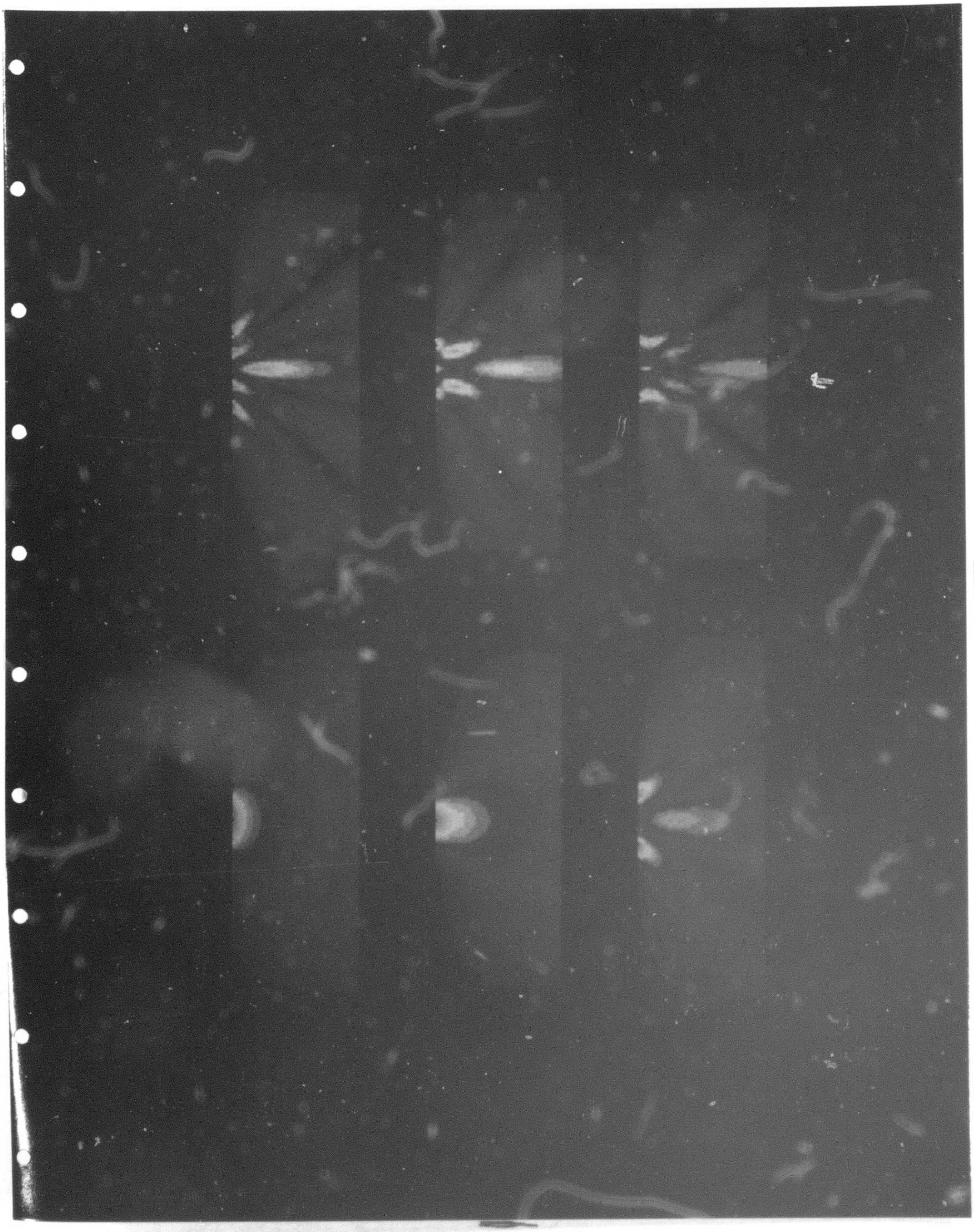

Figure 11. Comparison of the power density of the scattered field for the free surface with a bump as a function of the amplitude of the bump. All plots are scaled to absolute range (0.1, 3.0).

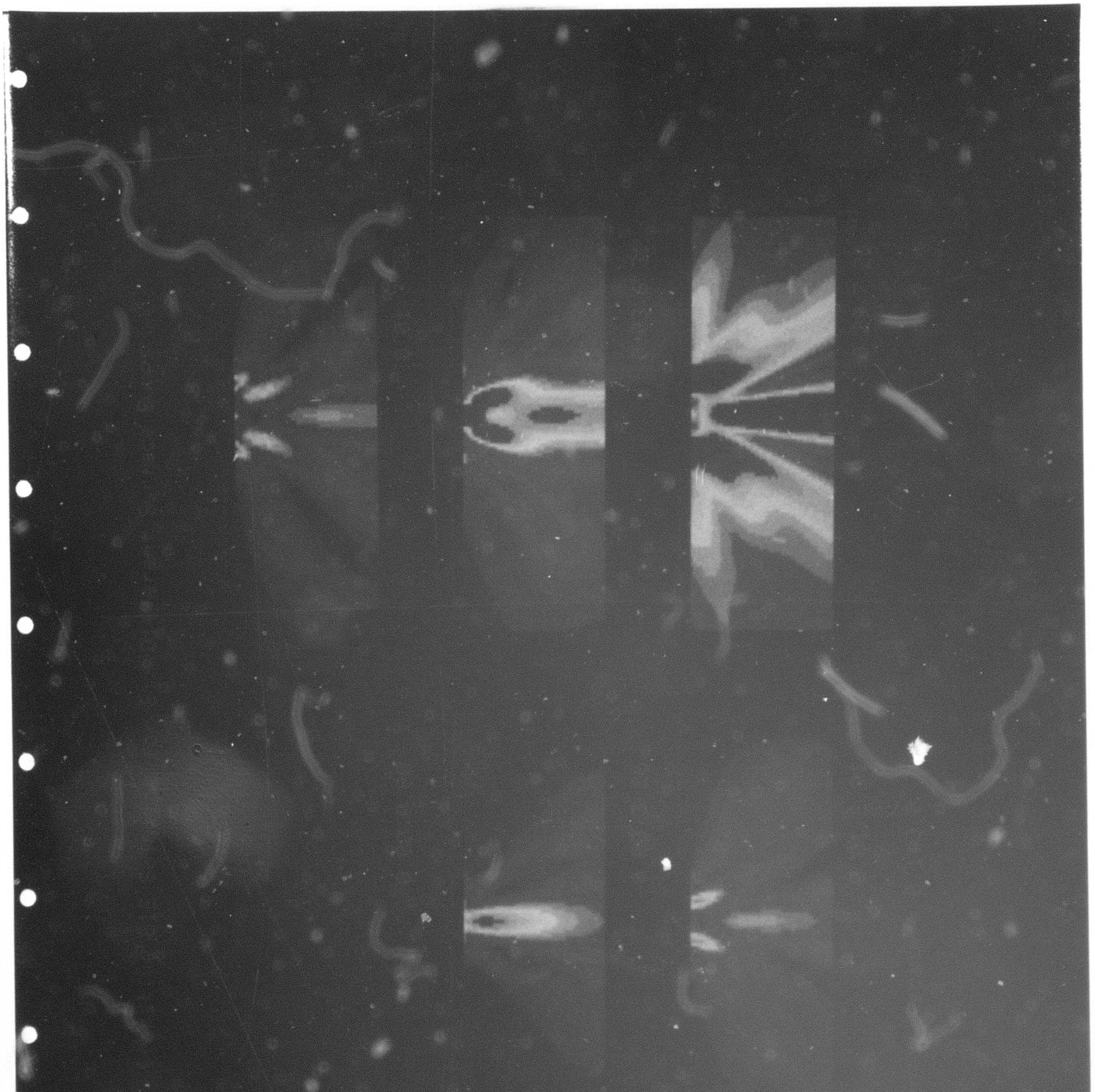

Figure 12. Corresponding results to Figure 11 in the time domain for a line of receivers located several grid dimensions below the free surface. All plots are scaled to absolute range (-1.0, 0.5).

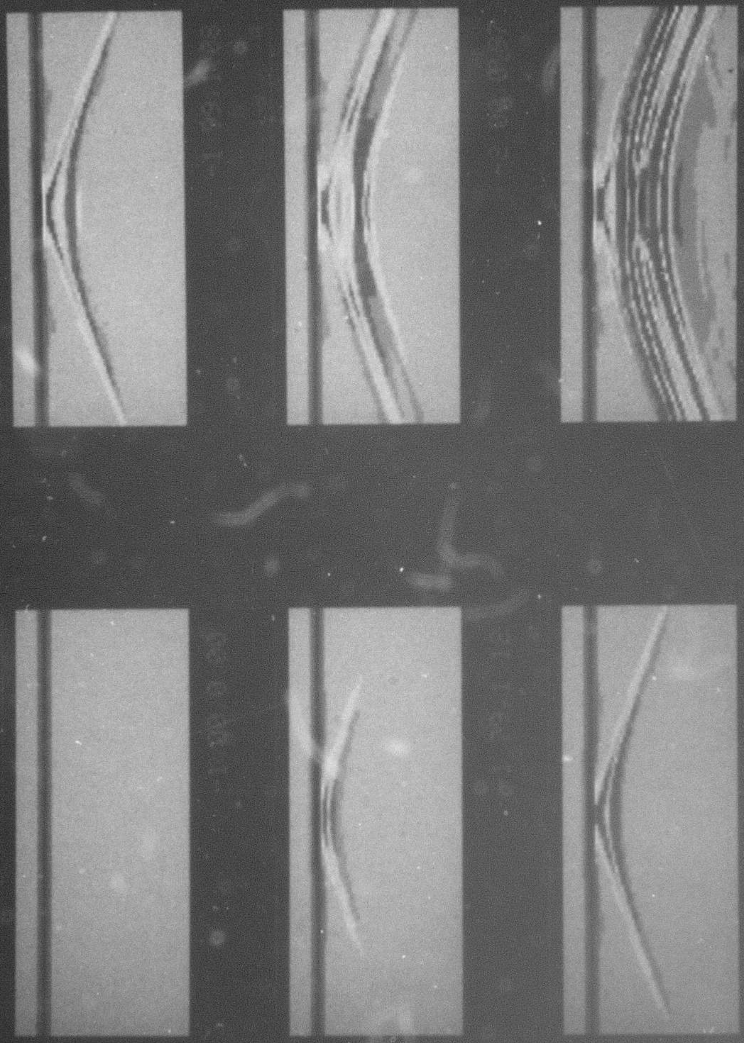

Figure 13. Power density of the scattered field due to a vertically incident plane wave impinging on a highly irregular free surface calculated with the iterative BIE technique at four different frequencies. All plots are self-scaled.

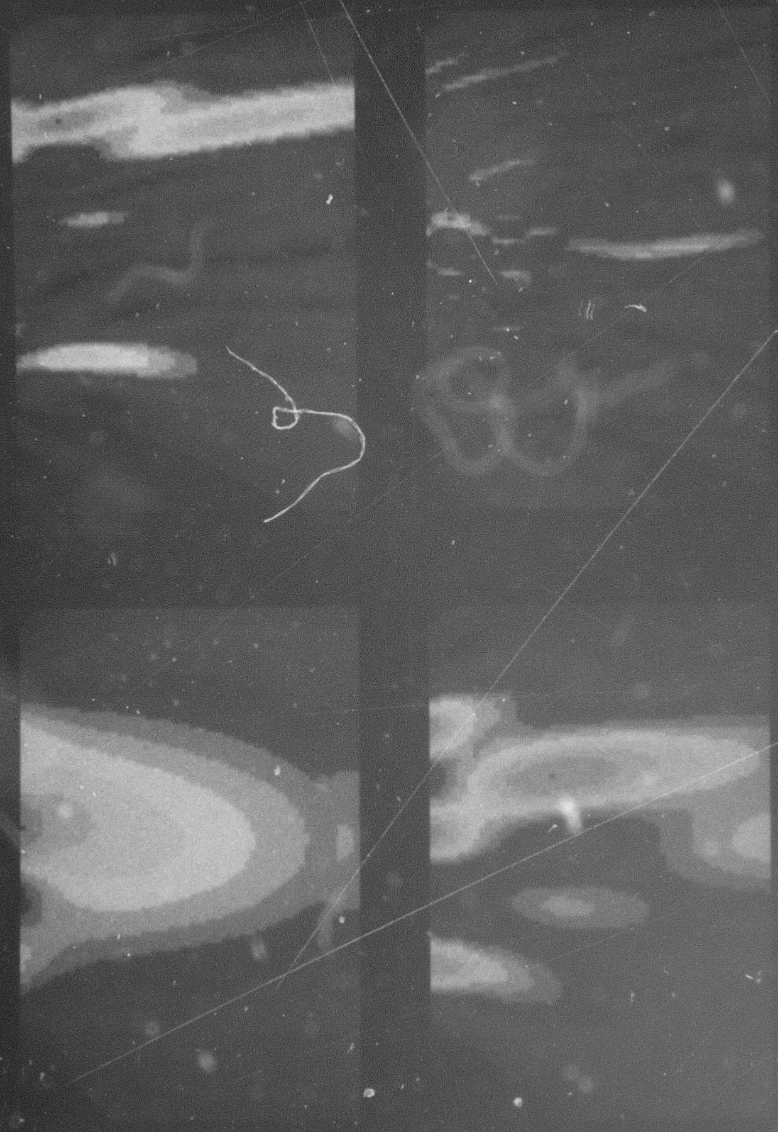

Figure 14. Analogous results to Figure 13 for a plane wave incident at 30 degrees from vertical. All plots are self-scaled.

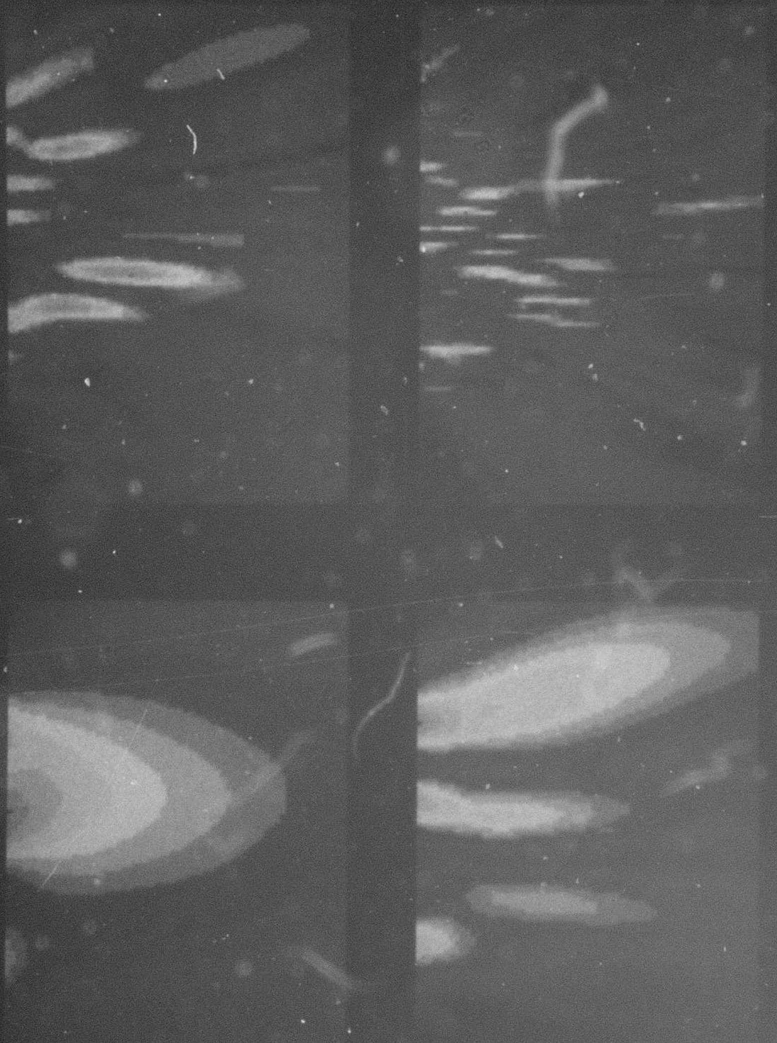

four different frequencies corresponding to wavenumbers of 0.1, 0.5, 1.0 and 2.0 in the upper left, lower left, upper right and lower right plots, respectively. As anticipated from the analogous sensitivity study in Figure 10 for the case of a simple bump irregularity, increasingly focussed reflections and diffractions are observed from the surface irregularities as the frequency is increased. Again, at low frequency, the wavelengths are approaching or exceeding the dimensions of the surface irregularities, which reduces the diffractive effects and causes the irregularities to resemble local point source emitters. Time sections for both angles of incidence considered in Figures 13 and 14 are displayed in Figure 15 for a line of receivers located just below the free surface. The normal incidence section is on the left and the oblique incidence section is on the right and are in the same format as the plots of Figures 9 and 12. As anticipated from the power density fields at the sampling of frequencies shown in Figures 13 and 14, all diffractive effects are accurately simulated in the iterative BIE solution and there are no spurious edge effects.

In Figure 16, the sensitivity of the time section for the obliquely incident plane wave case of Figure 15 is examined with respect to amplitude of the surficial irregularities. The four time sections represent the iterated BIE response compared with surficial irregularities of four different amplitudes, respectively. All four plots are displayed using the same absolute color scaling. In the lower left plot, the surficial irregularities are sufficiently small relative to the shortest wavelengths considered in the calculation that the scattered energy is negligible compared to the primary reflected wave. As the surficial irregularites are increased, the scattered energy increases and the diffracted waves are seen to be as large in absolute value as the primary reflected wave.

The case of propagation through an interface is considered in Figures 17 through 20. The first two of these figures demonstrate the accuracy of the iterative BIE technique for this case. In Figure 17, the power density of the scattered transmitted field through the interface is compared using the zero order BIE solution for an impedance contrast

Figure 15. Iterative BIE time domain solution corresponding to Figures 13 and 14 for a line of receivers located several grid dimensions below the free surface. Both plots are self-scaled.

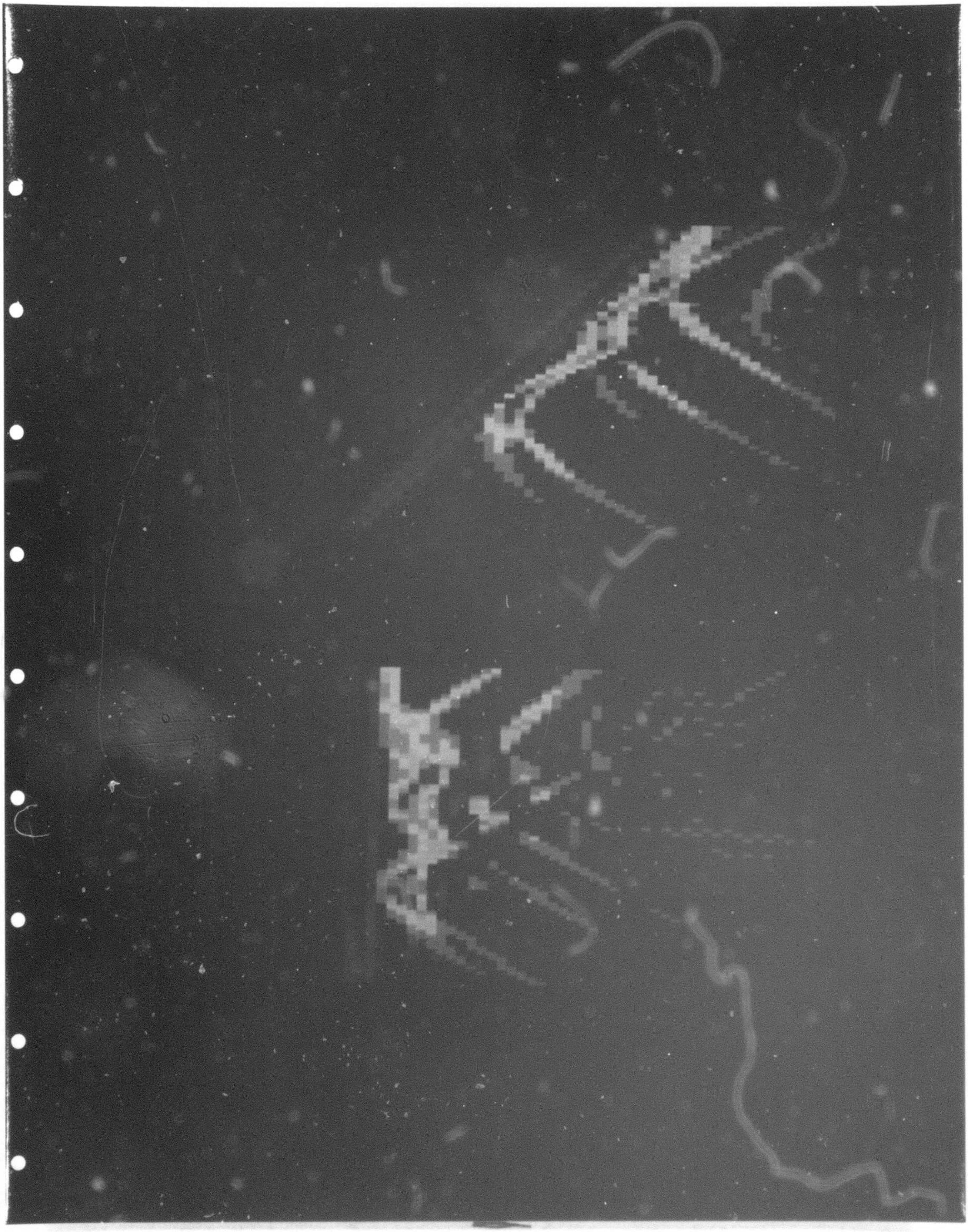

Figure 16. Comparison of iterated time domain solution for the highly irregular free surface as a function of the amplitude of the irregularities. All plots are scaled to absolute range (-1.0, 0.5).

ITERATIVE BIE TIME DOMAIN SOLUTION

Effect of Surface Irregularities

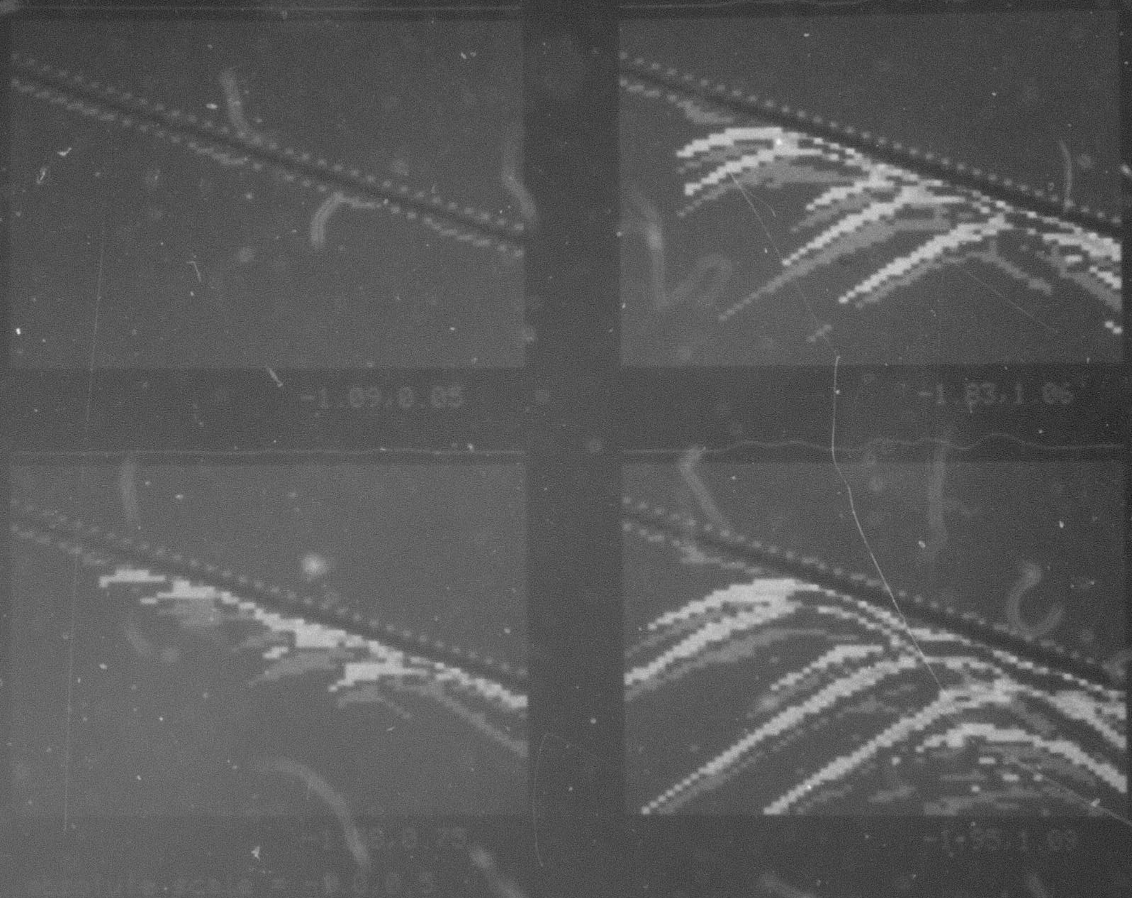

Figure 17. Comparison of power density of the scattered field due to propagation through an interface with and without an impedance contrast using the zero order BIE solution. Both plots are scaled to absolute range (0.0, 3.5).

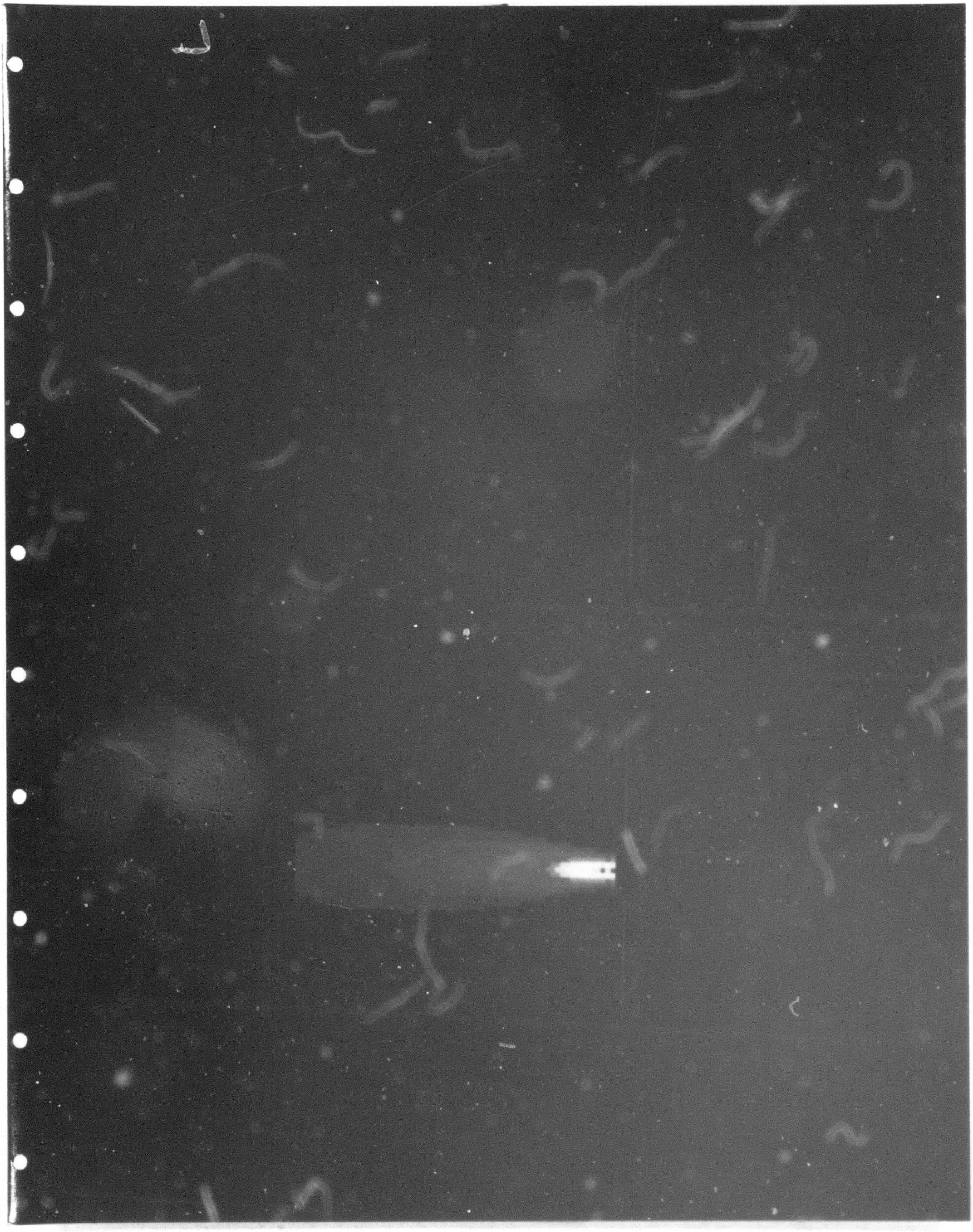

Figure 18. Magnification of power density of the scattered field for the zero impedance contrast case from Figure 17 as a function of iteration number, showing convergence to null solution. Both plots are scaled to absolute range (0.0, 0.2).

Figure 19. Power density of the scattered field due to propagation through an interface as a function of angle of plane wave emergence (critical angle at 30 degrees). All plots are self-scaled.

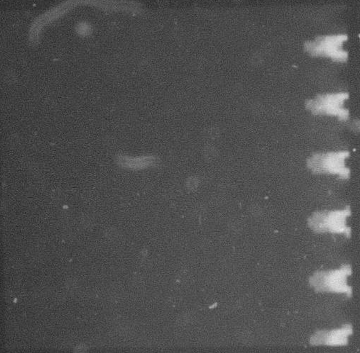
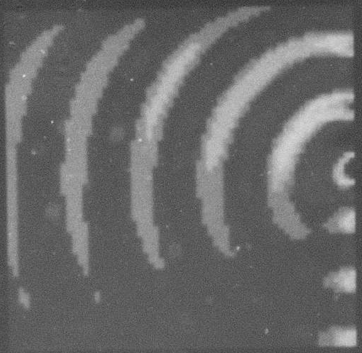
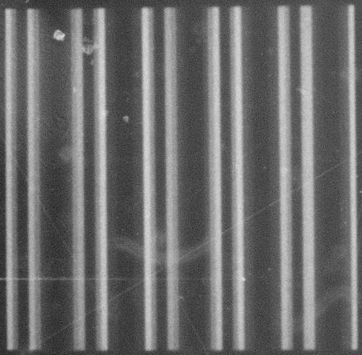
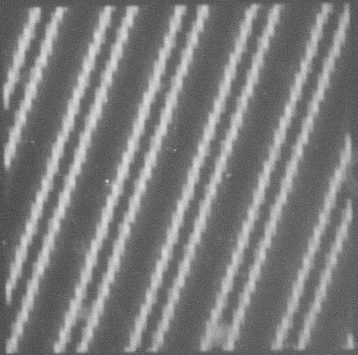

Figure 20. Power density of the scattered field due to propagation through an interface at intermediate and high frequencies. All plots are self-scaled.

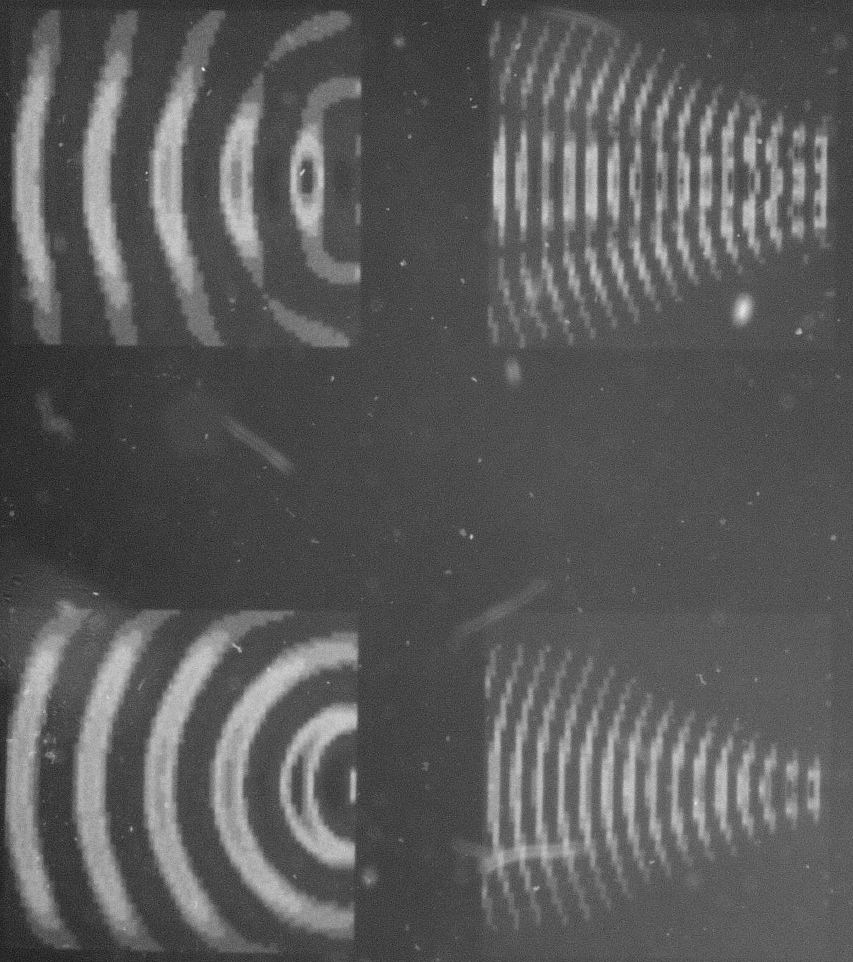

of 1.5 in the left plot and no impedance contrast in the right plot. Both plots are displayed on the same absolute color scale and as expected, no transmitted scattered energy is displayed for zero impedance contrast. The field for the zero impedance contrast case is magnified in the left plot of Figure 18 showing the numerically null solution. While the field is negligible compared to the finite impedance contrast case in Figure 17, the numerical solution is never exact. Fortunately, however, the iterated BIE solution converges to the exact solution as more and more iterations are performed as demonstrated in the right plot of Figure 18 with the next order iterated solution converging an order of magnitude closer to the exact solution.

In Figures 19 and 20, the acoustic velocity above the interface is twice the velocity below the interface, so that the critical angle of emergence is 30 degrees from vertical. The power density of the scattered transmitted field at an intermediate frequency is shown in Figure 19 as a function of emergence angle. As demonstrated by the sequence of plots for a planar interface from pre-critical emergence in the left column of plots to post-critical emergence in the upper right plot, the iterative BIE approach provides the correct results under all cases. In particular, the critically refracted waves in the upper right plot properly decay as a function of distance from the boundary (note that these waves can not be simulated using the approximate Kirchhoff solution technique). The post-critical case is repeated in the lower right plot for a simple non-planar interface. The important feature to notice is how the bump acts like a point source and radiates a significant amount of energy in the general direction of the incoming wave that would otherwise be absent as shown in the upper right plot. In the case of a multilayered half-space, irregularities along interfaces will give rise to late arriving head wave energy at the free surface that would otherwise not be evidenced with planar interfaces. In Figure 20, the power density of the scattered transmitted field due to normally incident propagation through simple non-planar interfaces is compared at intermediate and high frequency (three times intermediate value). The comparison is performed for irregular interfaces consisting of a single bump and a double bump in the left and right columns, respectively. The important feature to notice here is the significant beaming of the scattered field at high frequency (lower row of plots) in contrast to the simple point-source like emissions from the irregularity at low frequency.

The case of propagation through an irregular interface with a flat free surface overhead is considered in Figure 21. The acoustic velocity in the layer is half the value of the underlying half-space. The power density of the scattered field due to a vertically incident plane wave is compared at intermediate and high frequencies (twice the intermediate value) in the left and right plots, respectively, for a relatively thick layer. As in Figure 20, much more focussing is experienced at high frequency (right plot) and surface waves can be observed along the free surface at lower frequency (left plot) which decay exponentially as a function of depth for the thick layer. The center plot is the same as the left plot except that the layer thickness is considerably reduced giving rise to a large trapped surface wave propagating bilaterally away from the irregularity for the normally incident plane wave.

Figure 21. Power density of the scattered field due to propagation through an irregular interface with a flat free surface overhead. All plots are self-scaled.

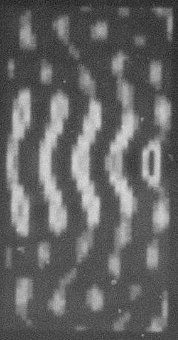

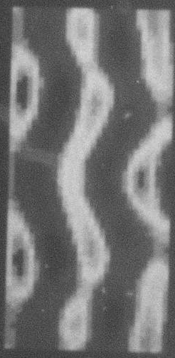

5.0 RECOMMENDED EXTENSIONS OF THE ITERATIVE BIE ALGORITHM

An iterative BIE algorithm has been developed for acoustic, two-dimensional structures having no more than a single irregular layer overlying a semi-infinite half space. The simplicity of the algorithm has allowed efficient testing of the methodology and refinement of the iterative procedure. Results for the simple cases supported under this algorithm were presented in Section 4.2 and are quite useful in providing new insights into wave propagation problems involving irregular interfaces. Now that the method has been shown to be reliable, complete and highly efficient (relative to finite difference type techniques), a more general iterative BIE algorithm is needed to study more complex wave propagation problems.

The formulation in Section 4.1 is completely general for an irregular, multilayered, elastic, three-dimensional half-space and the solution technique is outlined in detail. The most straightforward extension of the algorithm is to the case of a multilayered, two-dimensional half-space because the Green's functions are the same as for the single layer, 2-D case and the deconvolutional form of the BIE matrix equation can still be handled with one-dimensional Fourier transform techniques. However, the two-dimensional class of problems is limiting and the next recommended extension is to the three-dimension case. The extension to the full multilayered, 3-D case is straightforward in theory with the Green's functions simplifying to exponential functions from Hankel functions (refer to Appendix A) and with the deconvolutional form of the BIE matrix equations handled with two-dimensional Fourier transform techniques. The efficiency of the 3-D code will depend very strongly on optimized handling of the large core requirements and spatial gridding requirements as a function of frequency. It is anticipated that with sufficient effort on developmental efficiency, the code will execute up to an order of magnitude faster than finite difference type codes.

It is recommended that the matrix formalism be retained in all extensions of the algorithm to permit optimally efficient execution through use of array processing hardware if desired. Also, the elastic case should be explicitly supported as the form of algorithms is the same with just more bookkeeping required for the expanded set of nontrivial components at each node, and a number of source types should be explicitly supported including point forces, explosions, point dislocations, and finite sources.

6.0 REFERENCES

Apsel, R.J. (1979). *Dynamic Green's functions for layered media and applications to boundary-value problems*, Ph.D. Thesis, Univ. of Calif. at San Diego, 349 pp.

Berryhill, J.R. (1979). Wave equation datuming, *Geophysics*, *44*, pp. 1329-1344.

Cole, D.M. (1980). *A numerical boundary integral equation method for transient motions*, Ph.D. Thesis, Calif. Inst. of Tech., 228 pp.

deHoop, A.T., 1958. *Representation theorems for displacement in an elastic solid and their application to elastodynamic diffraction theory*, D.Sc. Thesis, Technische Hogeschool, Delft, The Netherlands.

Futterman, W.I. (1962). Dispersive body waves, *J. Geophys. Res.*, *67*, 5279-5291.

Hadley, D.M. (1982). *Theoretical and empirical studies of strong ground motion*, Final Report SGI-R-82-069 prepared for the United States Geological Survey, 86 pp.

Herrin, G., T. Goforth and J. Ferguson (1981). Semi-Annual technical report to the Air Force Office of Scientific Research.

Hong, T.L. and D.V. Helmberger (1978). Glorified optics and wave propagation in nonplanar structure, *Bull. Seism. Soc. Am.*, *68*, pp. 1313-1330.

Lundquist, G.M. and M.N.S. Kam (1982). *Relative receiver functions for the Eastern Kazakh Global Array and the Nevada Test Site Global Array*, Technical Report SGI-R-82-071 prepared for DARPA (Secret).

Mellman, G.R., R.S. Hart, G.M. Lundquist and D.M. Hadley (1982). *Investigations of near-source structural effects on body waves. Part I-Yucca Flats*, Technical Report SGI-R-82-058 prepared for DARPA, 59 pp.

Ohsaki, Y., 1973. On movements of a rigid body in semi-infinite elastic medium, *Proceedings of the Japan Earthquake Engineering Symposium*, Tokyo, 245-252.

Scheuster, J. (1983). *Boundary integral equations*, Ph.D. thesis in preparation, Columbia University.

Scott, P. and D.V. Helmberger (1983). Applications of the Kirchhoff-Helmholtz integral to problems in seismology, *Geophys. J.R. astr. Soc.*, *72*, pp. 237-254.

6.0 REFERENCES (continued)

von Seggern, D., and Blandford, R. (1972). Source time functions and spectra for underground nuclear explosions. Geophys. J. R. Astr. Soc., 31, 83-98.

APPENDIX A. Infinite-space Green's functions

Expressions for the infinite-space Green's functions are given in this appendix for two and three dimensional wave propagation problems in acoustic and elastic material. In each case, the displacement and stress fields at location $\vec{y}$ due to an impulsive point source at location $\vec{x}$ are presented as dimensionless quantities per unit force in the frequency domain for compatibility with the frequency domain BIE method.

1. Three-dimensional, elastic case

The dimensionless displacement field per unit force is given by

$$\begin{aligned}(4\pi\mu R)G_{\ell m}(\vec{x},\vec{y};\omega) &= [\hat{x}_{\ell m}(1+3d_\alpha) - \delta_{\ell m}d_\alpha]\gamma^2 e^{-ik_\alpha} \\ &\quad - [\hat{x}_{\ell m}(1+3d_\beta) - \delta_{\ell m}(1+d_\beta)]\, e^{-ik_\beta} \qquad \text{(A-1)}\end{aligned}$$

in which $G_{\ell m}(\vec{x},\vec{y};\omega)$ is the ℓ-component of the complex displacement field at location $\vec{y}$ and frequency ω due to a point source in the m-direction at location $\vec{x}$ with ℓ,m=1,2,3. The first main term on the right-hand side corresponds to the compressional wave traveling at a velocity α and the second main term corresponds to the shear wave traveling at a velocity β. The various quantitives appearing in Eq. A-1) are defined by the following relations:

$\vec{x} - (x_1,x_2,x_3)$ = source location; $\vec{y} = (y_1,y_2,y_3)$ = receiver location;

$R = |\vec{y}-\vec{x}| = [(y_1-x_1)^2 + (y_2-x_2)^2 + (y_3-x_3)^2\}]^{\frac{1}{2}}$;

$\hat{x}_{\ell m} = \hat{x}_\ell \hat{x}_m$; $\hat{x}_m = (y_m-x_m)/R$, m = 1,2,3 ;

$\delta_{\ell m}$ = 1 if ℓ=m; $\delta_{\ell m}$ = 0 if $\ell \neq$ m;

$\alpha^2 = (\mu+2\lambda)/\gamma$; $\beta^2 = \mu/\rho$; $\gamma = \beta/\alpha$

μ,λ = Lamé constants ; ρ = density ;

$k_\alpha = \omega/\alpha$; $k_\beta = \omega/\beta$; $i = (-1)^{\frac{1}{2}}$;

$d_\alpha = (ik_\alpha R)^{-1}\,[1+(ik_\alpha R)^{-1}]$; $d_\beta = (ik_\beta R)^{-1}\,[1+(ik_\beta R)^{-1}]$.

In the limit as source and receiver point coincide, R goes to zero causing singularities of the form R^{-j}, j=1,2,3 in $G_{\ell m}$. Conversely, in the limit as R goes to infinity, the near-field terms involving d_α and d_β vanish leaving a geometrical attenuation rate of (1/R). Material attenuation may be introduced by designating imaginary parts to the velocities α and β so that the exponential functions provide further decay at large distances. Also, these imaginary parts may be specified with arbitrary frequency dependence.

The corresponding dimensionless orders stress field per unit force is given by

$$\begin{aligned} 4\pi R^2 G_{\ell mn}(\vec{x},\vec{y};\omega) = {} & \Big\{ - \hat{x}_{\ell mn}[2\gamma^2(ik_\alpha R + 6 + 15d_\alpha)] \\ & + d_{\ell mn}[(2\gamma^2-1)ik_\alpha R + (4\gamma^2-1) + 6\gamma^2 d_\alpha] \\ & + (d_{\ell mn}+d_{mn\ell})[2\gamma^2(1+3d_\alpha)] \Big\} e^{-ik_\alpha R} \\ + & \Big\{ \hat{x}_{\ell mn}[2(ik_\beta R + 6 + 15d_\beta)] - d_{\ell mn}[2(1+3d_\beta)] \\ & - (d_{\ell nm}+d_{mn\ell})[ik_\beta R + 3 + 6d_\beta] \Big\} e^{-ik_\beta R} \end{aligned} \qquad \text{(A-2)}$$

in which $G_{\ell mn}(\vec{x},\vec{y};\omega)$ is the ℓm-component of the complex stress field at location $\vec{y}$ and frequency ω due to a point source in the n-direction at location $\vec{x}$ with ℓ,m,n = 1,2,3. Again, the first and second main terms on the right-hand side correspond to the compressional and shear waves, respectively. Those quantities appearing in Eq. (A-2) that were not used in Eq. (A-1) are defined by the following relations:

$$\hat{x}_{\ell mn} = \hat{x}_\ell \hat{x}_m \hat{x}_n \quad ; \quad d_{\ell mn} = \delta_{\ell m} \hat{x}_n \quad .$$

The *singularities in the* stress components $G_{\ell mn}$ are of the form R^{-j}, j=1,2,3,4 as R goes to zero which is one order higher than the corresponding singularities in the displacement components. However, the far-field geometrical (and material) attenuation behavior is the same as described for the displacements.

The ℓ-component of the complex traction field at location $\vec{y}$ is then obtained using Cauchy's formula by forming the dot product of the stress tensor with the unit normal vector $\vec{v}$ at that point:

$$H_{\ell n}(\vec{x},\vec{y};\omega) = G_{m\ell n}(\vec{x},\vec{y};\omega) \cdot v_m(\vec{y}) \quad , \quad m=1,2,3. \tag{A-3}$$

2. Three-dimensional, acoustic case

The dimensionless displacement field per urit force is given directly from Eq. (A-1) to read:

$$[4\pi(\lambda+2\mu)R]G_{\ell m}(\vec{x},\vec{y};\omega) = [\hat{x}_{\ell m}(1+3d_\alpha) - \delta_{\ell m}d_\alpha]\, e^{-ik_\alpha} \tag{A-4}$$

with the corresponding dimensionless stress field per unit force given directly from Eq. (A-2) to read:

$$\begin{aligned} 4\pi R^2 G_{\ell mn}(\vec{x},\vec{y};\omega) = \Big\{ & -\hat{x}_{\ell mn}[2\gamma^2(ik_\alpha R + 6 + 15d_\alpha)] \\ & + d_{\ell mn}[(2\gamma^2-1)ik_\alpha R + (4\gamma^2-1) + 6\gamma^2 d_\alpha] \\ & + (d_{\ell mn}+d_{mn\ell})[2\gamma^2(1+3d_\alpha)] \Big\}\, e^{-ik_\alpha R} \end{aligned} \tag{A-5}$$

The traction field may then be evaluated by introducing Eq.(A-5) into Eq. (A-4).

3. Two-dimensional elastic case

The Green's functions are presented for the two-dimensional case of antiplane strain. There is only one nonzero displacement component and one nonzero traction component for antiplane strain. Assuming that x_2 is the translational direction, the the dimensionless displacement component per unit force is given by

$$4\mu G_{22}(X_1,x_3;y_1,y_3;\omega) = -i\gamma^2 H_0^{(2)}(k_\alpha r) - iH_0^{(2)}(k_\beta r) \qquad \text{(A-6)}$$

in which $H_n^{(2)}$ is the Hankel function of the second kind of order n and $r = [(x_1-y_1)^2 + (x_3-y_3)^2]^{\frac{1}{2}}$. The corresponding dimensionless traction component per unit force is given by:

$$\begin{aligned} 4rH_{22}(x_1,x_3;y_1,y_3;\omega) &= ik_\alpha(y_3-x_3)H_1^{(2)}(k_\alpha r) \\ &+ ik_\beta(y_3-x_3)H_1^{(2)}(k_\beta r) \quad . \end{aligned} \qquad \text{(A-7)}$$

In this case, the singularities arising when source and receiver points coincide (r=0), occur for the displacement component in Eq. (A-6) in the imaginary part of the zero order Hankel function, exhibiting logarithmic behavior (i.e., Bessel function of the second kind $Y_0(z) \sim (2/\pi)\ln(z)$ as z approaches zero). For the stress components in Eq. (A-7), the singularities occur in the imaginary part of the Hankel functions of order 1 (i.e., Bessel function $Y_1(z) \sim -(2/\pi)/z$ as z approaches zero). The cases of plane strain or plane stress exhibit similar singularity behavior.

4. Two-dimensional acoustic case

The displacement and traction components are given directly from Eqs. (A-6) and (A-7) to read:

$$4(\lambda+2\mu)G_{22}(x_1,x_2;y_1,y_3;\omega) = -iH_0^{(2)}(k_\alpha r) \qquad \text{(A-8)}$$

$$4rH_{22}(x_1,x_3;y_1,y_3;\omega) = ik_\alpha(y_3-x_3)\ H_1^{(2)}(k_\alpha r) \quad . \qquad \text{(A-9)}$$